TRANSPORTATION CORRIDOR RESILIENCY IN THE FACE OF A CHANGING CLIMATE

FINAL PROJECT REPORT

by

Keith Cunningham, PI - University of Alaska Fairbanks
Michael J. Olsen, Co PI – Oregon State University,
Joseph Wartman, Co-PI – University of Washington,
Ben Leshchinsky, Co-PI –Oregon State University,
Matt O'Banion, Graduate Student – Oregon State University

for
Pacific Northwest Transportation Consortium (PacTrans)
USDOT University Transportation Center for Federal Region 10
University of Washington
More Hall 112, Box 352700
Seattle, WA 98195-2700

and the
Alaska University Transportation Center, Alaska Department of Transportation

and in cooperation with the
US Department of Transportation-Research and Innovative Technology Administration (RITA)

Disclaimer

The contents of this report reflect the views of the authors, who are responsible for the facts and the accuracy of the information presented herein. This document is disseminated under the sponsorship of the U.S. Department of Transportation's University Transportation Centers Program, in the interest of information exchange. The Pacific Northwest Transportation Consortium, the U.S. Government and matching sponsor assume no liability for the contents or use thereof.

Technical Report Documentation Page

1. Report No.	2. Government Accession No.	3. Recipient's Catalog No.
2013-M-UAF-0042		

4. Title and Subtitle	5. Report Date
Transportation Corridor Resiliency in the Face of a Changing Climate - Final Project Report	11/29/2017
	6. Performing Organization Code

7. Author(s)	8. Performing Organization Report No.
Keith W. Cunningham – University of Alaska Michael J. Olsen – Oregon State University Joseph Wartman – University of Washington Ben Leshchchinsky – Oregon State University Matt O'Banion – Oregon State University	

9. Performing Organization Name and Address	10. Work Unit No. (TRAIS)
PacTrans Pacific Northwest Transportation Consortium University Transportation Center for Region 10 University of Washington More Hall 112 Seattle, WA 98195-2700	**11. Contract or Grant No.** DTRT13-G-UTC40

12. Sponsoring Organization Name and Address	13. Type of Report and Period Covered
United States of America Department of Transportation Research and Innovative Technology Administration	Research 11/01/2016 - 12/31/2017
	14. Sponsoring Agency Code

15. Supplementary Notes

Report uploaded at www.pacTrans.org

16. Abstract

The effects of a changing climate on transportation corridor slopes are poorly understood, but several recent studies have suggested that landslide activity, especially rockfall, is likely to increase as a consequence of the increased occurrence of intense precipitation events. Effects from climate change such as extreme temperature fluctuations, freeze-thaw cycles, and increased rainfall quantity and intensity weaken geologic materials, exacerbating slope failures. In order to understand slope rockfall activity and its linkages to weather and climate, we acquired additional high-resolution lidar data and unmanned aircraft systems structure data from motion surveys of rock slopes in Alaska. Over several projects we have successively developed a rich data set spanning 5 years to quantitatively evaluate rockfall activity (the magnitude-frequency of rockfall events), which proved useful for examining correlations with historic weather patterns and future climate forecasts. As part of this research, we further developed the Rockfall Activity Index (RAI) and began to evaluate how the RAI can be linked to increasing temperature swings and freeze-thaw cycles. This quantitative approach for rockfall activity forecasting is an important step in providing tools to state departments of transportation to assess transportation corridor risks, sustainability, and resiliency, especially for Alaska in the face of a changing climate. This research is a first step in providing the analysis tools needed to meet a recent presidential directive and help improve our fundamental understanding of the potential impacts of climate change on the safety of and mobility within transportation networks in landslide-prone regions such as the Pacific Northwest in the U.S.

17. Key Words:	18. Distribution Statement
Lidar, Rockfall Activity Index (RAI),	No restrictions.

19. Security Classification (of this report)	20. Security Classification (of this page)	21. No. of Pages	22. Price
Unclassified.	Unclassified.	TBD	NA

Form DOT F 1700.7 (8-72) **Reproduction of completed page authorized**

METRIC (SI*) CONVERSION FACTORS

APPROXIMATE CONVERSIONS TO SI UNITS

Symbol	When You Know	Multiply By	To Find	Symbol
		LENGTH		
in	inches	25.4		mm
ft	feet	0.3048		m
yd	yards	0.914		m
mi	Miles (statute)	1.61		km
		AREA		
in^2	square inches	645.2	millimeters squared	cm^2
ft^2	square feet	0.0929	meters squared	m^2
yd^2	square yards	0.836	meters squared	m^2
mi^2	square miles	2.59	kilometers squared	km^2
ac	acres	0.4046	hectares	ha
		MASS (weight)		
oz	Ounces (avdp)	28.35	grams	g
lb	Pounds (avdp)	0.454	kilograms	kg
T	Short tons (2000 lb)	0.907	megagrams	mg
		VOLUME		
fl oz	fluid ounces (US)	29.57	milliliters	mL
gal	Gallons (liq)	3.785	liters	liters
ft^3	cubic feet	0.0283	meters cubed	m^3
yd^3	cubic yards	0.765	meters cubed	m^3
Note: Volumes greater than 1000 L shall be shown in m^3				
		TEMPERATURE (exact)		
°F	Fahrenheit temperature	5/9 (°F-32)	Celsius temperature	°C
		ILLUMINATION		
fc	Foot-candles	10.76	lux	lx
fl	foot-lamberts	3.426	candela/m^2	cd/cm^2
		FORCE and PRESSURE or STRESS		
lbf	pound-force	4.45	newtons	N
psi	pound-force per square inch	6.89	kilopascals	kPa

These factors conform to the requirement of FHWA Order 5190.1A *SI is the symbol for the International System of Measurements

APPROXIMATE CONVERSIONS FROM SI UNITS

Symbol	When You Know	Multiply By	To Find	Symbol
		LENGTH		
mm	millimeters	0.039	inches	in
m	meters	3.28	feet	ft
m	meters	1.09	yards	yd
km	kilometers	0.621	Miles (statute)	mi
		AREA		
mm^2	millimeters squared	0.0016	square inches	in^2 m^2
meters squared		10.764	square feet	ft^2 km^2
kilometers squared		0.39	square miles	mi^2 ha
hectares (10,000 m^2)		2.471	acres	ac
		MASS (weight)		
g	grams	0.0353	Ounces (avdp)	oz
kg	kilograms	2.205	Pounds (avdp)	lb mg
megagrams (1000 kg)		1.103	short tons	T
		VOLUME		
mL	milliliters	0.034	fluid ounces (US)	fl oz
liters	liters	0.264	Gallons (liq)	gal
m^3	meters cubed	35.315	cubic feet	ft^3
m^3	meters cubed	1.308	cubic yards	yd^3
		TEMPERATURE (exact)		
°C	Celsius temperature	9/5 °C+32	Fahrenheit temperature	°F
		ILLUMINATION		
lx	lux	0.0929	foot-candles	fc
cd/cm^2	candela/m^2	0.2919	foot-lamberts	fl
		FORCE and PRESSURE or STRESS		
N	newtons	0.225	pound-force	lbf
kPa	kilopascals	0.145	pound-force per square inch	psi

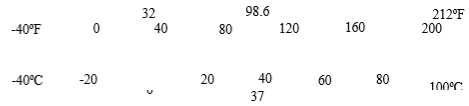

Table of Contents

Table of Figures

Acknowledgments

The research team acknowledges Oregon DOT providing matching funds to support this project and Alaska DOT for providing assistance with permits. Shane Markus (UW), Dr. Chris Parrish (OSU), Nicholas Forfinski, and Pat Teagarden (Terrasond) assisted with the field data collection. Lecia Geosystems, David Evans and Associates, and Maptek I-Site provided equipment and/or software to support this research.

List of Abbreviations

DEM	Digital elevation model
DOT	Department of transportation
DSM	Digital surface model
DTM	Digital terrain model
FHWA	Federal Highway Administration
GCP	Ground control points
GNSS	Global Navigation Satellite System
Lidar	Light detection and ranging
NOAA	National Oceanic and Atmospheric Administration
PRA	Probabilistic Risk Assessment
RAI	Rockfall Activity Index
RCP	Representative carbon pathway
RDA	Rockslope Deterioration Assessment
REF	Rockslope Evolution Framework
RHRS	Rockfall Hazard Rating System
SfM	Structure from motion
SNAP	Scenarios Network for Alaska + Arctic Planning
TLS	Terrestrial laser scanning
UAS	Unmanned aircraft system

Executive Summary

The Office of Management and Budget's Circular A-11 directed federal agencies—including transportation agencies—to consider climate preparedness and resilience as part of their FY 2017 construction and maintenance budget requests. The effects of a changing climate on transportation corridor slopes are poorly understood, but several recent studies (e.g., Hicks, 1995; Occhiena and Pirrulli, 2012) suggest that landslide activity, especially rockfall, is likely to increase as a consequence of the increased occurrence of intense precipitation events. Changing climate is associated with an increased variability in temperature swings and precipitation. A Federal Highway Administration (FHWA, 2016) review cited research indicating "extreme temperature fluctuations and freeze-thaw cycles can weaken [geologic materials] and increase susceptibility to slope failures."

In order to understand slope rockfall activity and its linkages to weather and climate, we acquired additional high-resolution lidar surveys of rock slopes in Alaska. This Pacific Northwest Transportation Consortium (PacTrans)-supported research successively developed a rich data set to quantitatively evaluate rockfall activity (the magnitude-frequency of rockfall events), which proved useful for examining correlations with historic weather patterns and future climate forecasts. As part of this research, we further developed the Rockfall Activity Index (RAI) and began to evaluate how the RAI can be linked to increasing temperatures swings and freeze-thaw cycles. We also developed a new approach to model slope changes with time that calculates evolving erosion patterns on the cliff years into the future. The model also shows how the RAI and other morphological patterns change across the slope with time as material is unleashed from the cliff. The model has the ability to change the rockfall rates over time on the basis of environmental factors.

This quantitative approach for rockfall activity forecasting is an important step in providing tools to state departments of transportation to assess transportation corridor risks, sustainability, and resiliency, especially for Alaska in the face of a changing climate. This research is a first step in providing the analysis tools needed to meet a recent presidential directive and help improve our fundamental understanding of the potential impacts of climate change on the safety of and mobility within transportation networks in landslide-prone regions such as the Pacific Northwest in the U.S.

Chapter 1 Climate Change and Transportation Resiliency

Interest in transportation infrastructure in the Arctic region is growing because of increased maintenance costs that can be linked to climate change. Alaska is seeing increased ground subsidence and slope instability at twice the rate of the mid-latitudes (National Climate Assessment, 2016). Because much of Alaska's transportation infrastructure is developed on permafrost, the region's deeper thaws and other extreme weather events are likely to incur significant costs for mitigation and repair.

As an example, the impacts of landslides, thaw-induced subsidence, and rockfalls on infrastructure have cost $11 million/year for Alaska (Connor and Harper, 2013), $10 million for Oregon (Burns and Madin, 2009), and $15 million/year for Washington (Washington DNR, 2016), sometimes resulting in hundreds of millions of dollars of losses during extreme events (e.g., the Oso, Washington, landslide of 2014).

The U.S. National Climate Assessment indicates that risks to Alaska infrastructure could be substantially greater (Larson et al., 2008), with costs reaching $5.6 to $7.6 billion by 2080 for all forms of transportation infrastructure (figure 1.1).

A recent report from the National Academies of Science (2016) conclusively demonstrated that climate change has led to an increase in the frequency and intensity of daily temperature extremes and has contributed to a widespread intensification of daily precipitation extremes (Scott, 2016). Precipitation extremes and longer-term climate change trends are forcing departments of transportation (DOTs) to anticipate asset management issues by assessing vulnerability and risk to assets. This includes identifying vulnerable facilities and systems, changing maintenance practices, and "right-sizing" infrastructure retrofits such as bridges and culverts for future operational conditions.

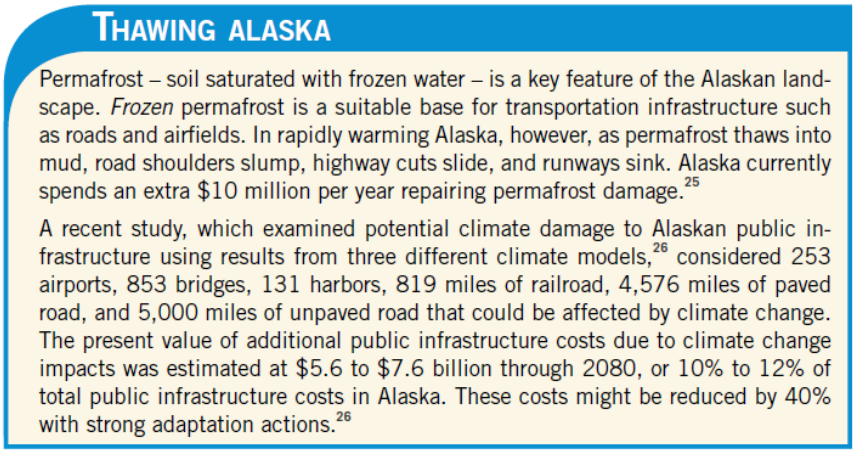

THAWING ALASKA

Permafrost – soil saturated with frozen water – is a key feature of the Alaskan landscape. *Frozen* permafrost is a suitable base for transportation infrastructure such as roads and airfields. In rapidly warming Alaska, however, as permafrost thaws into mud, road shoulders slump, highway cuts slide, and runways sink. Alaska currently spends an extra $10 million per year repairing permafrost damage.[25]

A recent study, which examined potential climate damage to Alaskan public infrastructure using results from three different climate models,[26] considered 253 airports, 853 bridges, 131 harbors, 819 miles of railroad, 4,576 miles of paved road, and 5,000 miles of unpaved road that could be affected by climate change. The present value of additional public infrastructure costs due to climate change impacts was estimated at $5.6 to $7.6 billion through 2080, or 10% to 12% of total public infrastructure costs in Alaska. These costs might be reduced by 40% with strong adaptation actions.[26]

Figure 1.1 Thawing Alaska, from US National Climate Assessment: Estimating future costs for Alaska public infrastructure at risk from climate change. Page 132. (Larsen et al., 2008).

These aspects of transportation planning are collectively known as "resilience and adaptation" and are now part of the DOT vocabulary. Adaptation is not necessarily new, as there have always been challenges of unstable soils, rockfall, flooding, and extreme heat. What are new are the increased frequency and intensity of these events and their increasing economic impacts. Adequate planning and response are needed to ensure the resilience of communities that are dependent on critical transportation networks. The impending challenge for state transportation agencies is not in the distant future, and the Federal Highway Administration (FHWA) is urging state agencies to implement climate change adaptation programs to assess vulnerability and the risk of geohazards on infrastructure (FHWA, 2016).

The geography, demographics, and development history of Alaska have led to limited transportation corridors without any network redundancy. This means that the state's transportation network is vulnerable to disruption. The state also has limited capacity to adapt to events such as rock falls, landslides, and damage to culverts and bridges from storm events.

Since 2012, we have been acquiring high-resolution lidar surveys of close to 20 rock-slopes in Alaska in support of Pactrans-supported studies of roadway safety and geotechnical

asset management. The setting for this research is fortuitous, since Alaska is regarded a climate change field laboratory by experts who have found that the region is already experiencing the early effects of a rapidly changing climate (Larsen et al., 2008). In this project, we capitalized on this treasure trove of unique, high-resolution data to quantify how rockfall activity (i.e., the magnitude-frequency of rockfall events) varied with changes in annual storm intensity and other meteorological and climatic indices from 2012 to 2016. We also utilized this information with a landslide activity magnitude-frequency forecasting procedure (Barlow et al., 2012) to investigate how the safety and resiliency of transportation corridors may change over their design lives as a result of climate alteration.

This research is a first step in providing the analysis tools needed to meet a presidential directive and also to help improve our fundamental understanding of the potential impacts of climate change on the safety of transportation networks in landslide-prone regions. It directly aligns with the 2016 PacTrans theme of "Safe Infrastructure: High tech solutions to lifeline resilience." Specifically, it addresses PacTrans' research priority of using new data-driven technologies to improve the safety and resilience of transportation systems in the Northwest United States. Landslides pose a well-recognized threat to the safety of motorists throughout much of the mountainous terrain of the Pacific Northwest (e.g., Badger and Lowell, 1992). This research also addresses a critical research need that was identified this year by the FHWA (2016): to understand better the "link between rockfalls, weather events, and climate change."

Chapter 2 Assessing Rockfall in the Face of Climate Change

Assessing rockfall and landslide risk poses challenges when DOT's decide where to allocate funds, especially from a system-wide asset management perspective with limited DOT budgets. Slope assessment has traditionally been laborious and costly. Current best practices for management do not necessarily facilitate proactive methods for slope data collection, analysis, and management to identify and remediate hazardous conditions before a failure occurs.

Another factor limiting slope assessment has been inadequate data and observation systems. This is especially true for Alaska, primarily because of its vast and austere environment. Without baseline data and monitoring systems, analysis of the changing factors that affect transportation infrastructure is unfeasible. To overcome this limited understanding, PacTrans and its cost-share partners agreed to begin a baseline laser-scan survey at two critical locations in Alaska deemed most likely to face rockfall and landslide events. In 2012, a first round of field surveying collected slope morphology and geology data at two field sites in Alaska, known as Long Lake and Glitter Gulch. Laser scans using light detection and ranging (lidar) equipment were the first step in evaluating the magnitude and frequency of rockfall activity. This first set of scans was completed using mobile laser scanning technology.

2.1 Rockfall Activity Index

Subsequent scans using terrestrial laser scan technology in 2013 (Phase II), 2014 (Phase II), 2015 (Phase III), and 2017 (this project phase) have now created a rich data set that can be used to develop a more precise and quantifiable geohazard risk assessment. To quantify rockfall activity and assess landslide risk, the PacTrans research team developed the Rockfall Activity Index (RAI) (Dunham et al., 2017). The RAI is a point cloud-derived, high-resolution, morphology-based method for assessing rockfall hazards. The RAI is applied in a two-step

procedure. In the first step, morphological indices (local slope and roughness derived from a high-resolution, three-dimensional point cloud) are used as an indicator to classify erosion and mass wasting processes acting on rock slopes. In the second step, the slope morphology classifications are used with estimated instability rates to map rockfall activity across a slope face. The RAI method has been implemented as a simple and computationally efficient algorithm, which makes it repeatable and easy to apply across rock slopes of virtually any size.

The method provides an estimate of rockfall kinetic energy release (this is the numerical Rockfall Activity Index, RAI) along 1-m rock slope segments, as well as detailed mapping of rock slope morphology and kinetic energy release areas. The RAI does not consider large, structurally controlled failures such as rock slides or topples, which are typically assessed with limit equilibrium analysis procedures. The RAI is expressed as annual cumulative delivery of rockfall kinetic energy (kJ) at the base of a unit length (1-m) slope. Although this quantitative formulation suggests a high degree of engineering precision, it should be recognized that variability and uncertainty exist in the parameters used to compute the RAI. Thus the term "index" was selected to emphasize the method's intended use as a measure of rockfall activity, rather than an exact predictor of annual energy release from rock slope.

2.2 Rockfall Activity Index in the Face of Climate Change

To further the development of the RAI, this round of the PacTrans research had the following objectives:

- Acquire an additional dataset from a 2017 campaign for further analysis and to create a longer time series data set for climate change trend analysis.
- Compare data from the digital surface models to corroborate rockfall trends.
- Compare rockfall trends with historic weather to validate climatic forecast trends.

We then examined correlations between the quantifiable Rockfall Activity trends with the historic weather patterns of the study sites. Forecasted climatic trends for the rest of the 21st century were also examined.

Chapter 3 Review of Phases I to III of the PacTrans Research

PacTrans is an organization that sponsors university transportation research in the Pacific Northwest. Located at the University of Washington, its partner institutions include universities in Alaska, Oregon, and Idaho. Phases I to IV (the current phase) of this research were led by the University of Alaska Fairbanks, with co-investigators from Oregon State University and the University of Washington. Note that each phase was a separate project with unique research goals, but each effectively built upon the results of the previous phases and leveraged previously collected data to maximize the return on investment. This section highlights key research findings and products from the previous phases that laid the groundwork for this current phase.

During the first phase, two critical transportation corridors in Alaska (figure 3.1) were selected for the research; they are colloquially known as Glitter Gulch and Long Lake. The Long Lake corridor is approximately half way between Anchorage and Glennallen on the Glenn Highway (mileposts 78 to 89). Glitter Gulch is located on the Parks Highway (mileposts 239 and 247), about halfway between Anchorage and Fairbanks. Glitter Gulch is immediately north of the tourist village at the entrance to the Denali Park, hence the kitschy name.

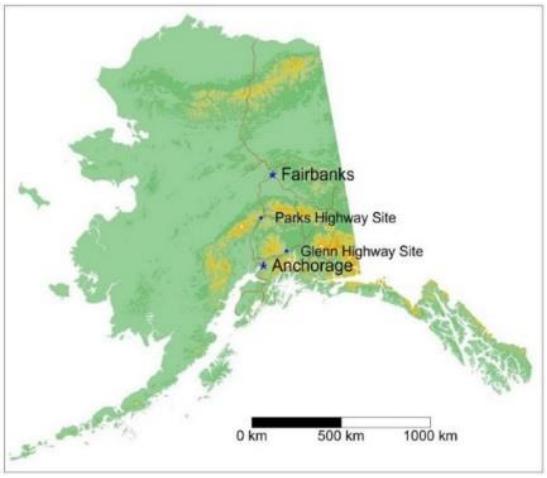

Figure 3.1 Locations of rockfall study sites in Alaska

3.1 Phase I Research Results

Phase I research had the objective of evaluating the capabilities of lidar data to assess slope hazards and risk in a geotechnical asset management framework and developing tools to use them. The research was conducted from fall 2012 to fall 2013. Using both mobile and static terrestrial lidar, it created a baseline of laser scanning measurements for 10 miles of highway at the Long Lake and Glitter Gulch sites with problematic slopes. Data from the laser scans were used to create detailed morphological models of the slopes, as well as a colorized lidar point cloud from cameras attached to the lidar scanners. The models helped to visualize a variety of geologic features, including rock types, fracturing, weathering, and talus accumulations. The slope morphology was of particular interest in the digital surface models (DSM), especially the rock cantilever overhangs that indicate slope surfaces with greater probabilities of slope instability. The mobile lidar data at Glitter Gulch were showcased on the November-December 2014 cover of TR News (figure 3.2).

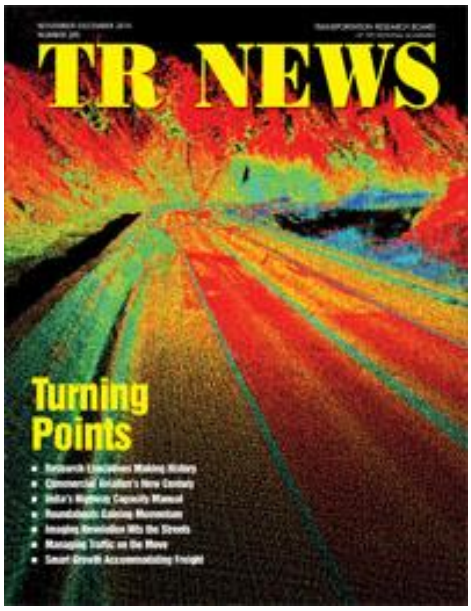

Figure 3.2 Lidar point cloud of the Glitter Gulch study site on the cover of *TR News* (Link at: http://onlinepubs.trb.org/onlinepubs/trnews/trnews295.pdf)

Three limitations to the mobile lidar scanning techniques were revealed, primarily involving insufficient scan detail (resolution) from the currently available technology when the lidar is traveling at highway speeds, vegetation interfering with scan data, and the blocking (occlusion) of laser scans by shadows cast by barriers, guard rails, and vegetation. However, the benefits identified included efficient coverage across large sections of highway, safe data collection, and the ability of the data to be utilized for multiple purposes in addition to slope assessment were identified.

The final report for the Phase I of the project (Metzger et al., 2012) is available at: http://depts.washington.edu/pactrans/wp-content/uploads/2012/12/PacTrans-2-739439-Metzger-Andrew-Multi-Project.pdf

3.2 Phase II Research Results

A scientific shortcoming determined in Phase I was that existing rockfall hazard assessment models were inadequate for the detailed lidar digital elevation model (DEM) data because they were too coarse. Both the Rockfall Hazard Rating System (RHRS) (Pierson, 1991 and Huang et al., 2009) and the Rockslope Deterioration Assessment (RDA) (Nicolson, 2004) are subjective, resulting in qualitative descriptions and risk assessments. A quantitative risk model exists called the Probabilistic Risk Assessment (PRA) (Bedford and Cooke, 2001), but it is also limited to subjective interpretation of slope instabilities. Without quantitative risk assessments, these models cannot produce analytic results using lidar DSM data sets as forecasting inputs.

The Phase I research also indicated that research into slope stability risk analysis could benefit from additional lidar scan data from another timeframe at a similar resolution, in order to perform slope change analysis. (The mobile laser scan data were difficult to compare with the

static scan data, given the differences in resolution.) The field survey during this phase focused on a narrower set of specific sites rather than attempting to capture data for the long sections of highway, as done in the first phase.

Change detection can identify specific locations of individual rockfall activity, talus accumulation, minute volumetric changes of the slope, overall volumetric change, and overall trends in morphology. Examples are provided in figures 3.3 and 3.4. This temporal analysis could then be further developed with more data to examine more complex phenomena, such as geologic fracturing, insolation on south facing slopes, freeze-thaw cycles, soil ratcheting, and the mitigation effects resulting from regular DOT slope maintenance. Measurement of rockslope change was the first step in developing a rockslope stability model capable of quantitative forecasts.

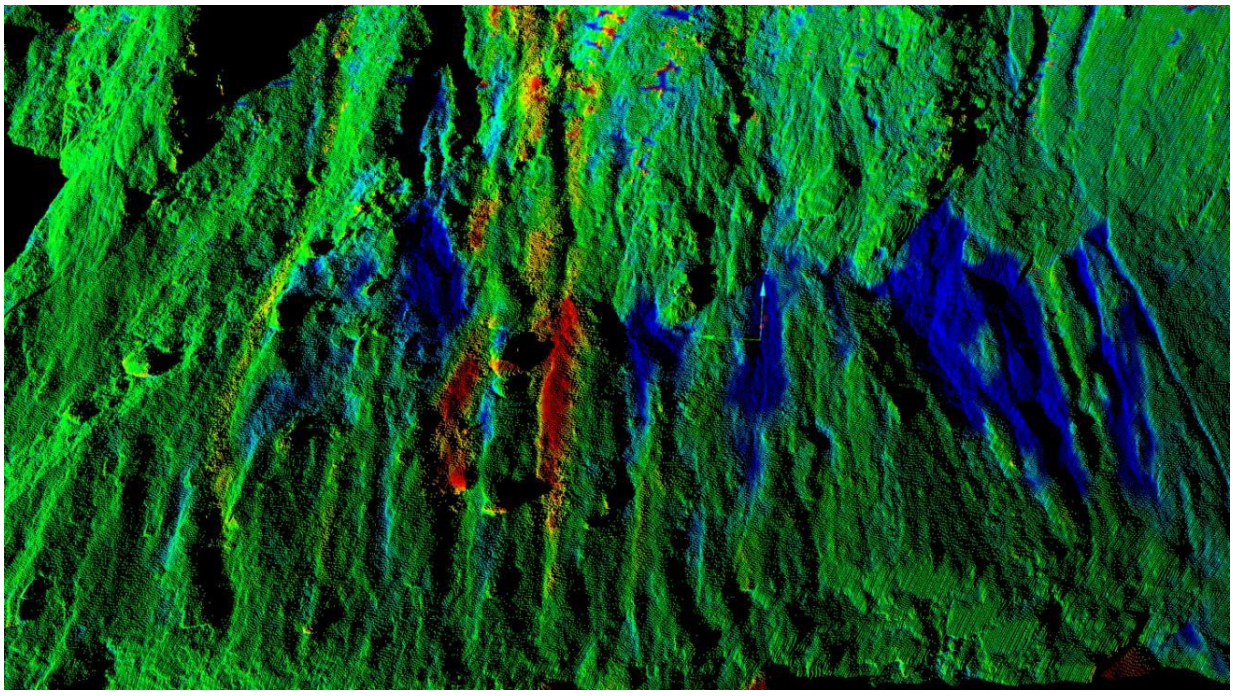

Figure 3.3 DEM change detection – red rock loss and blue rock accretion

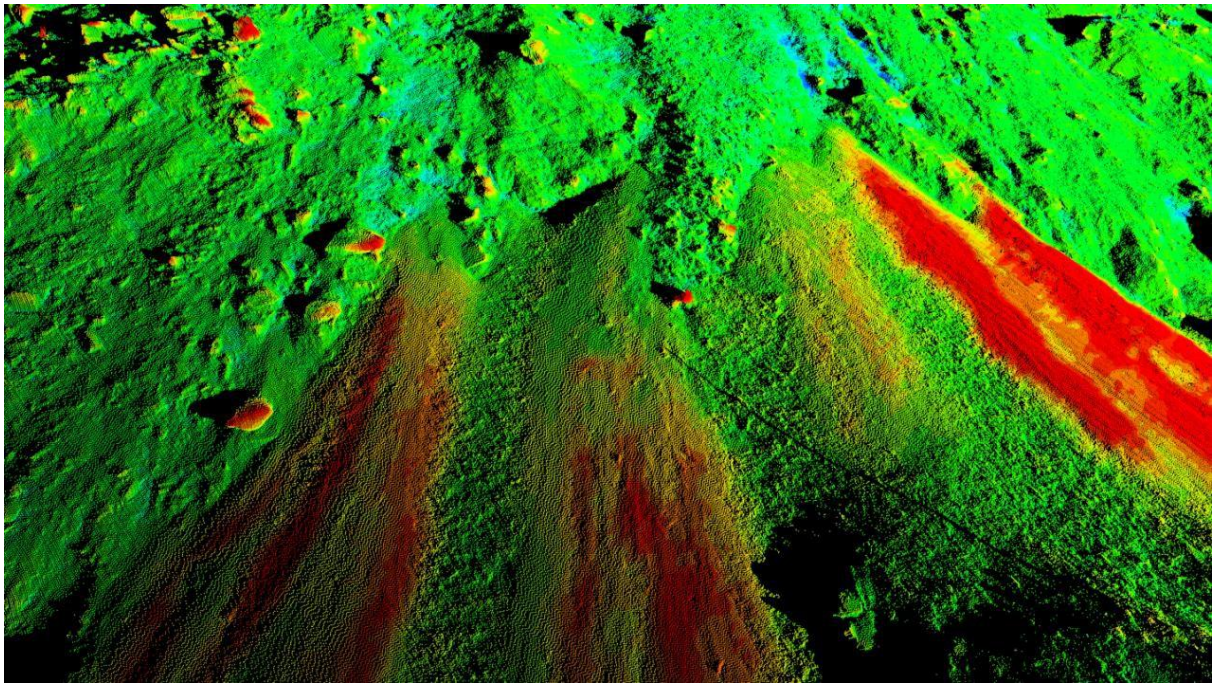

Figure 3.4 Close-up of eroded material at the talus (red < -0.25m) at Glitter Gulch

Cantilever overhangs and other complex features created scanning occlusions in the DEM, thus helping to focus the team's investigation on scientific solutions to scanning occlusions. Important research into how to help interpolate across the occluded scan data led to the publication of the paper titled, "To Fill or Not to Fill: Sensitivity Analysis of the Influence of Resolution and Hole Filling on Point Cloud Surface Modeling and Individual Rockfall Event Detection." (Olsen et al., 2015). This paper also presented an automated approach to detecting individual rockfall clusters to automate the development of magnitude frequency curves.

The ability to measure changes in slope surfaces and quantify them with precise detail led the team to an enhanced analysis of slope stability and the impacts of rock structure and weathering. By tracking morphology, it is also possible to quantify slope roughness across multiple scales. Changes in morphology and roughness can be precisely calculated to infer changes in slope volumetrics and the kinetic energy released with the slope change. These

components became part of the Rockfall Activity Index (RAI) developed to model slope dynamics.

The scientific methods and RAI were published in scholarly articles and in the PacTrans Phase II report. These links are at:

- The PacTrans Phase II Report (Cunningham et al., 2013): http://depts.washington.edu/pactrans/wp-content/uploads/2013/11/PacTrans_42-UAF-Cunningham.pdf
- Rockfall Activity Index in Engineering Geology (Dunham et al., 2017): http://www.sciencedirect.com/science/article/pii/S0013795216305671

3.3 Phase III Research Results

PacTrans sponsored the team's Phase III research with a new project to evaluate the quality of additional photogrammetric data collected via a drone (unmanned aircraft system or UAS) in addition to a third set of repeat terrestrial laser scans. The additional data also helped the team develop a quantifiable rockfall and slope stability model utilizing change detection techniques to forecast future slope behavior. This research effort also provided an opportunity to further test and refine the RAI system to support the point clouds acquired from drones.

Two important outcomes resulted from this phase. First was a detailed examination of the photogrammetry data captured by an off-the-shelf drone, which indicated that the resulting photogrammetry surface models were comparable to the lidar scans in many ways and of reasonable accuracy for slope morphology assessment, provided that adequate survey control was provided.

The photogrammetry process, called structure-from-motion (SfM), uses the motion parallax of the drone's changing position to generate detailed three-dimensional models of the

slope surfaces. While the SfM technique is not necessarily new, its application to terrain modeling is new, especially with the perspective that an airborne platform can achieve over-terrestrial imaging. The drone demonstrated that its "aloft" perspective generates DSM data of critical cantilever overhangs. Additionally, the point cloud density of the SfM model is comparable to that of the lidar scanner but was also found to be more consistent. Finally, unlike the lidar, which could only be operated from a narrow road shoulder, the drone proved able to quickly fly above the road and in an offset position from the target, making it safer to operate while collecting high quality data in a shorter amount of time (accounting for time required for survey control).

Rigorous comparison of the drone SfM data to terrestrial laser scan (TLS) data required rigorous survey control. Geodetic Global Navigation Satellite System (GNSS) receivers and total stations with targets serving as ground control points (GCP) placed on the slope were therefore necessary for both the drone photogrammetry and the lidar scanning.

The last step in the photogrammetry research was to fuse the drone DEM with the lidar DEM. The results were effective, with the drone data filling occlusions in the lidar data, and the lidar data helping to "control" the draping of the drone DSM point cloud. Thus a denser and more complete DEM was generated for the Phase III data collection without the problematic occlusions from the rock cantilever overhangs.

Project results were highlighted as a success story in the Pactrans Newsletter (figure 3.5). The project report for this phase will be forthcoming on the Pactrans website.

SUCCESS STORY #1: Cunningham, Unmanned Aircraft System Assessments of Landslide Safety for Transportation Corridors

Investigators: PI Keith Cunningham (UAF), Co-PI Michael Olsen (OSU), Co-PI Joe Wartman (UW)

Project Type: Multi-Institution Project

Title of Original Research: Unmanned Aircraft System Assessments of Landslide Safety for Transportation Corridors

Research Description: Over the last year this team has be using drones to collect optical imagery of several unstable slopes located in Alaska, using digital cameras to characterize and model slope stability and to forecast their dynamics.

Technology Transfer: "With this recent success," says Dr. Cunningham, "we can demonstrate this emerging survey technology that promises faster and more efficient data collection of slopes along transportation corridors." Thus they have applied for, and received, additional PacTrans funding for Technology Transfer. Their transfer will include the creation of a short promotional video of the research to showcase the effectiveness of drone imaging collection.

Figure 3.5 PacTrans Success Story.
(Link at: http://depts.washington.edu/pactrans/wp-content/uploads/2016/03/PacTrans-Fall-2015-Edition-14-Newsletter-Final.pdf)

Chapter 4 Current Phase (IV) Research Results

This Phase IV project had several primary goals. First was the collection of another round of rockslope data at the Glitter Gulch and Long Lake sites. A second goal was to conclude an in-depth analysis of the accuracy of the digital surface model (DSM) with terrestrial laser scan (TLS) data and structure-from-motion (SfM) data with survey control (expanding on Phase III). Third, the time series data were evaluated for changes in magnitude frequency curves. Fourth, an RAI forecasting model was developed to show the evolution of the slopes with time. Fifth and last, the DSM data from the scans were analyzed to determine whether historic weather trends could be correlated to slope retreat and then to examine how future climatic forecasts for the region might indicate a continuation of the observed patterns.

4.1 Step 1: Data Collection

The survey campaign was conducted in late summer of 2017. This included both a drone SfM (figure 4.1) and TLS (figure 4.2), with rigorous survey controls utilizing total station (Leica TS15, figure 4.3), GNSS (Leica GS14, figure 4.4), and survey targets for ground control points (GCP). New TLS equipment (Leica P40) was used for data collection, improving the data quality as well as providing denser, three-dimensional point clouds in a similar amount of time. In particular, the system had less noisy data from mixed pixels, resulting in the capture of clearer, sharper edges on the rock than the previous surveys. The same drone and camera combination was used as in the Phase III data collection, thus providing three-dimensional SfM models that were similar to those from before. Figures 4.5 and 4.6 provide example results of the TLS data and subsequent processing to determine the RAI.

Figure 4.1 Example drone operation with the flight controller (right) and the image acquisition software (left)

Figure 4.2 Example terrestrial laser scan set-up with the Leica P40 at a Glitter Gulch site.

Figure 4.3 Example operation of the total station at a Glitter Gulch site to acquire reflectorless measurements on the cliff face.

Figure 4.4 Example GNSS survey observation on a ground control point used to provide geo-referencing information for the total station.

(a)

(b)

(c)

Figure 4.5 (a) Overview of RGB colored terrestrial laser scans for Site LL85.5 with detailed close-ups (b and c).

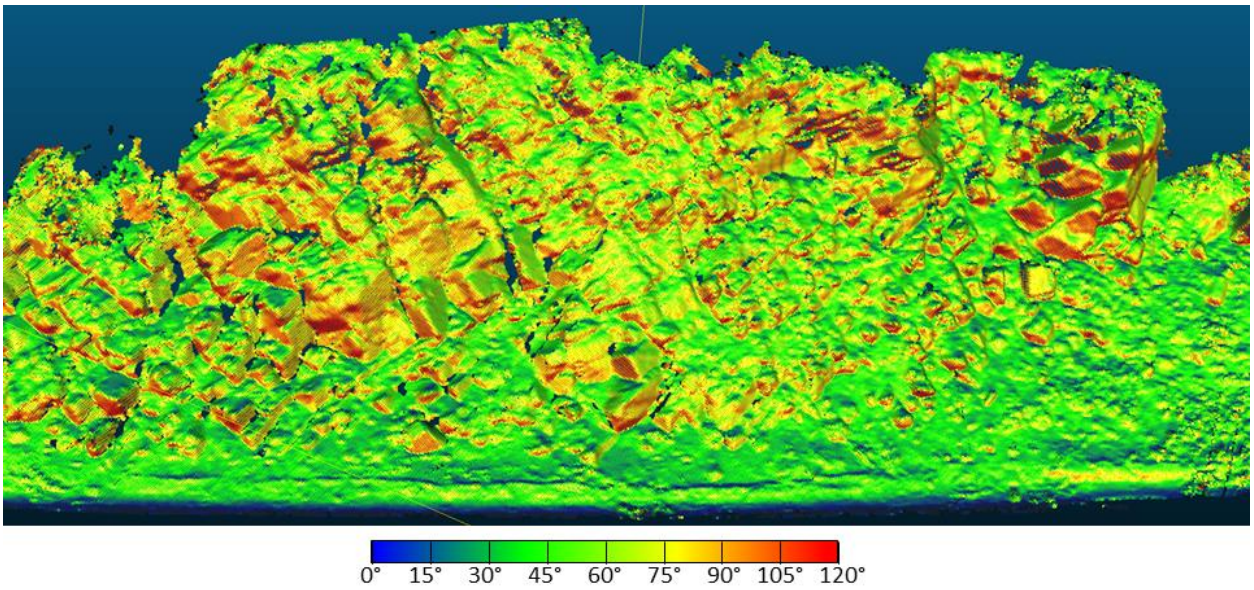

(a) Slope

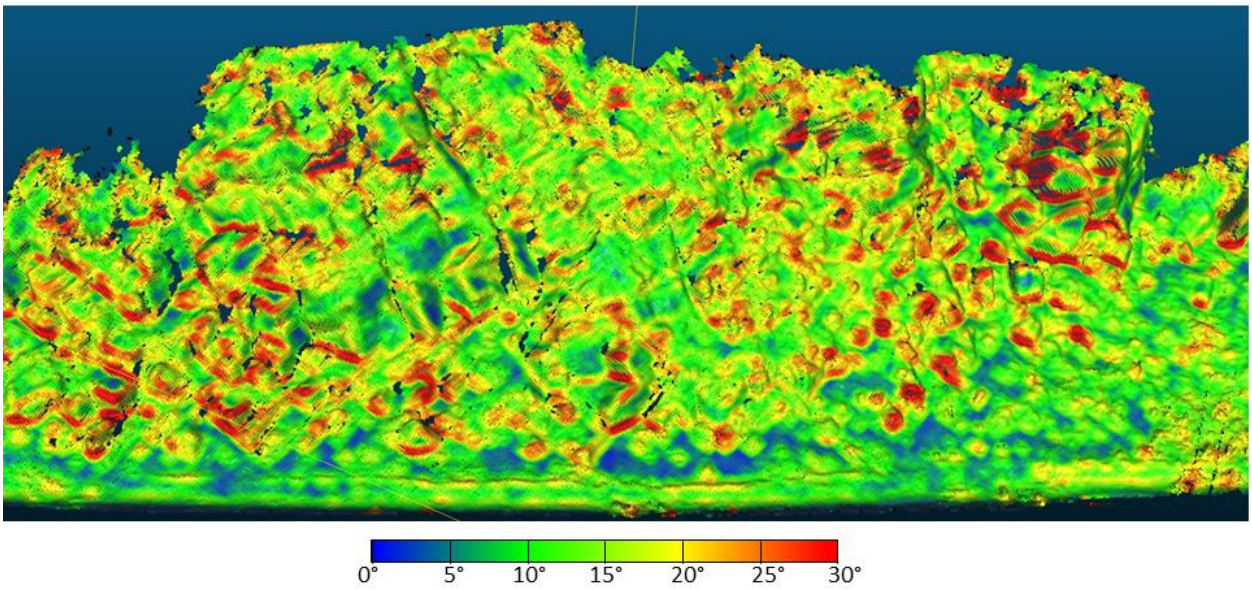

(b) Roughness (35cm)

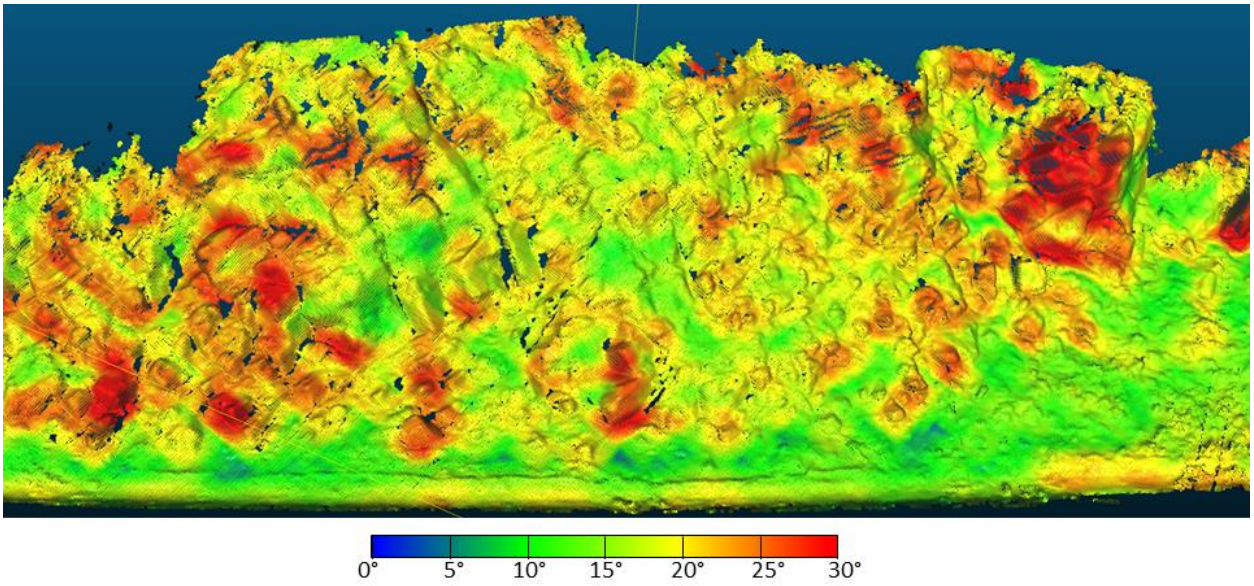

(c) Roughness (85 cm)

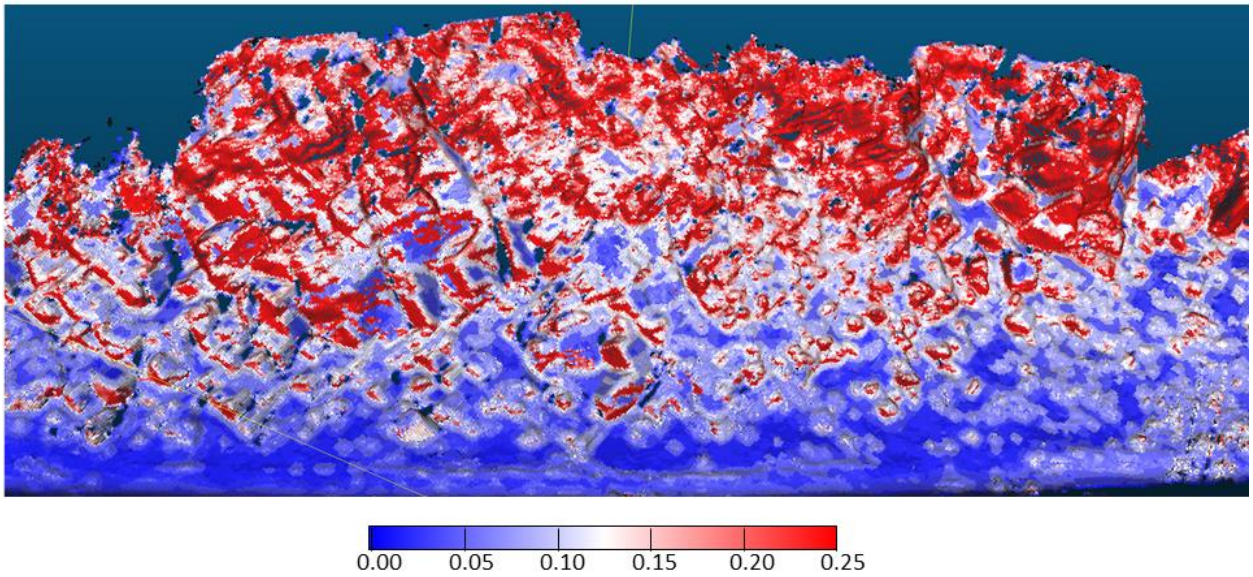

(d) Kinetic energy (kJ)

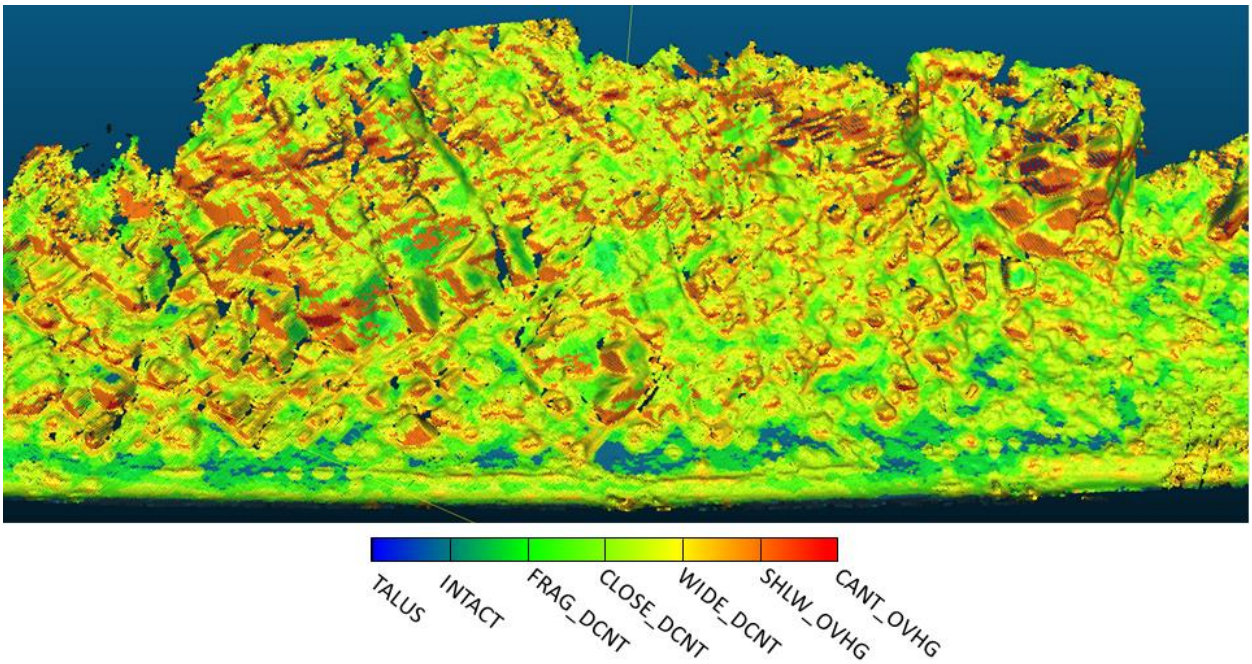

(e) RAI classification

Figure 4.6 Example calculations for Site LL85.5, including (a) Slope, (b) Roughness 35 cm, (c) roughness 85 cm, (d) Kinetic energy potential, and (e) Rockfall Activity Index

4.2 Step 2: Lidar SfM Comparison

The accuracy assessment comparing the TLS with the SfM data was rigorously conducted at three rock slopes at the Long Lake study site with variable morphologies and geometries. These are indicated by markers labeled RS1 (RockSlope 1), RS2, and RS3 in figure 4.7. While preliminary evaluations were conducted in Phase III, this phase enabled us to complete a much more in-depth analysis of the capabilities and limitations of the UAS-based SfM.

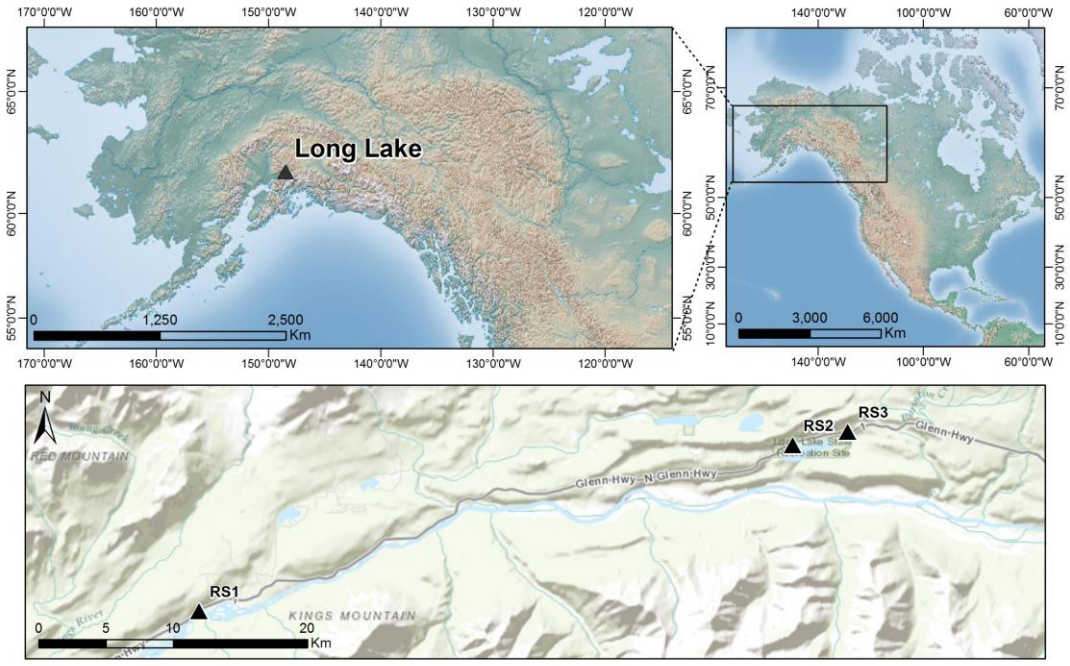

Figure 4.7 Study plan with three rockslopes selected: RS1, RS2, and RS3.

Figure 4.8 shows the colorized digital surface model (DSM) for each rock slope (RS1, RS2, and RS3), with black and white pattern targets used as ground control points (GCPs). The GCPs were used to survey the DSM with a total station linked to the geodetic network via GNSS receiver. The GCPs were also used to register the SfM data on top of the TLS data.

Further details and findings of this comparison are available in the manuscript (O'Banion et al., in press) provided in Appendix A, which was a product of this research project. Key findings included the following:

(1) UAS SfM models require significant survey control to provide results of significant accuracy for slope morphology assessment.

(2) The inclusion of ground-based photographs to supplement the UAS photographs significantly helps improve the models.

(3) SfM models offer some benefits in more consistent resolution and improved coverage across the slope.

(4) A challenge with UAS using SfM models for tall rock slopes is the difficulty of placing survey control on the upper section of the slope, leading to error propagation. For the SfM data collected in this phase, we remediated these effects by using a total station to sight indistinct features on the cliff and obtain reflectorless measurements to improve the model quality. (Note this approach had not yet been implemented for the comparison discussed in Appendix A.)

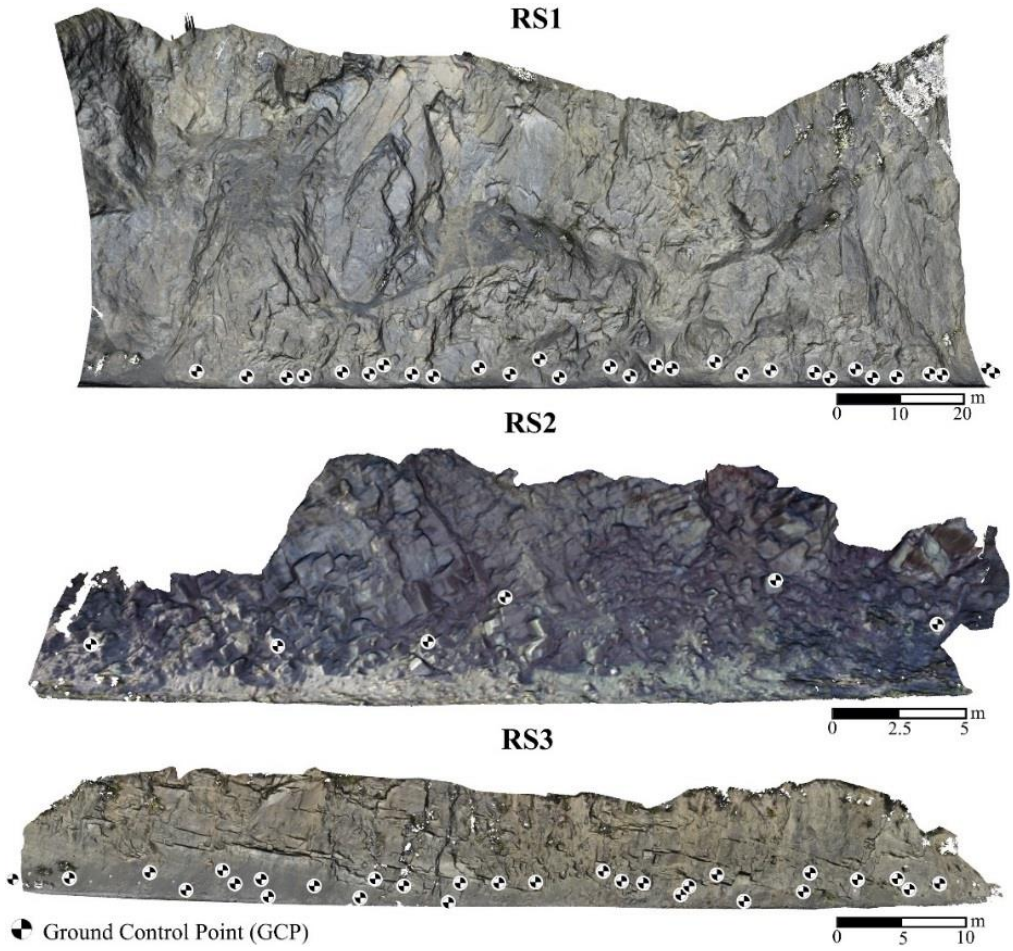

Figure 4.8 SfM-derived 5-cm surface models of the three rock slopes (RS1, RS2, and RS3) with the layout of black and white targets used as ground control points

4.3 Step 3: Development of Magnitude Frequency Curves

Change detection-derived magnitude–frequency relationships were developed for the Long Lake and Glitter Gulch rock slope study sites. These study sites provided an ideal test-bed setting for developing magnitude–frequency relationships because of their high rates of rockfall activity. Over 20 individual sites were evaluated in the study; however, for brevity, magnitude–frequency relationships are presented for four of the Long Lake sites (corresponding to approximate milepost locations 71, 88.5, 86.9, and 87). Figures 4.9 to 4.12 present cumulative magnitude–frequency relationships for three approximately one-year epochs (2012-2013, 2013-2014, and 2014-2015). The relationships included slight characteristic "rollover" for small volumes, as well as linearity in log-log space across several orders of magnitude of volume. The rollover phenomenon in landslide magnitude–frequency relationships was attributed to data censuring that occurred when survey resolutions were approached. The deviation from log-log linearity for large volumes has been noted by others and was attributed to the temporal censuring that occurred over relatively short monitoring time periods. The results were relatively consistent over the three year (2012-2015) monitoring period. Moreover, there was a general consistency across all the sites over this period, suggesting regular rates of rockfall activity at the Long Lake road cuts.

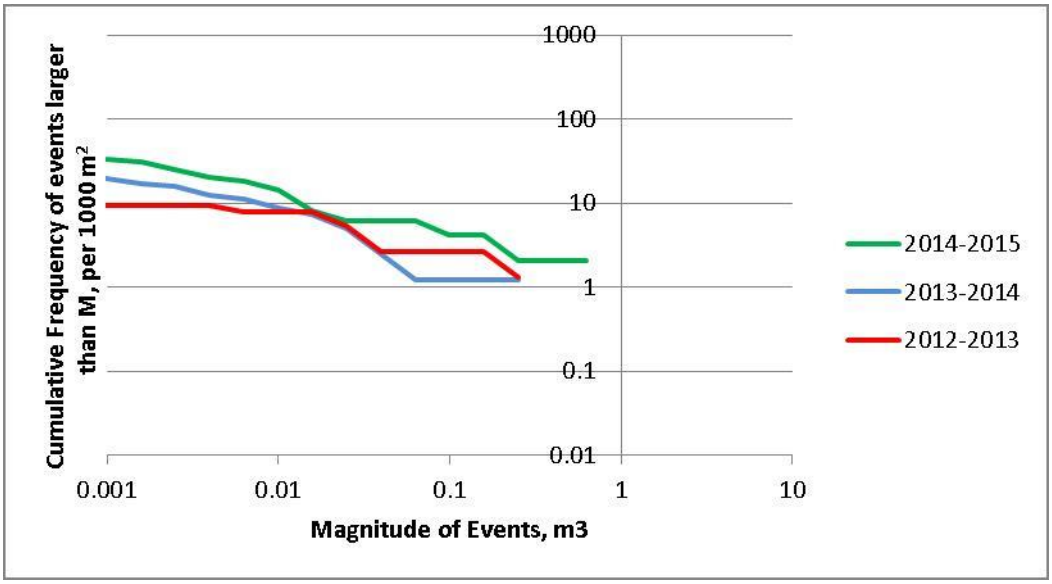

Figure 4.9 Cumulative magnitude–frequency relationships for three approximately 1-year epochs at site LL85.5

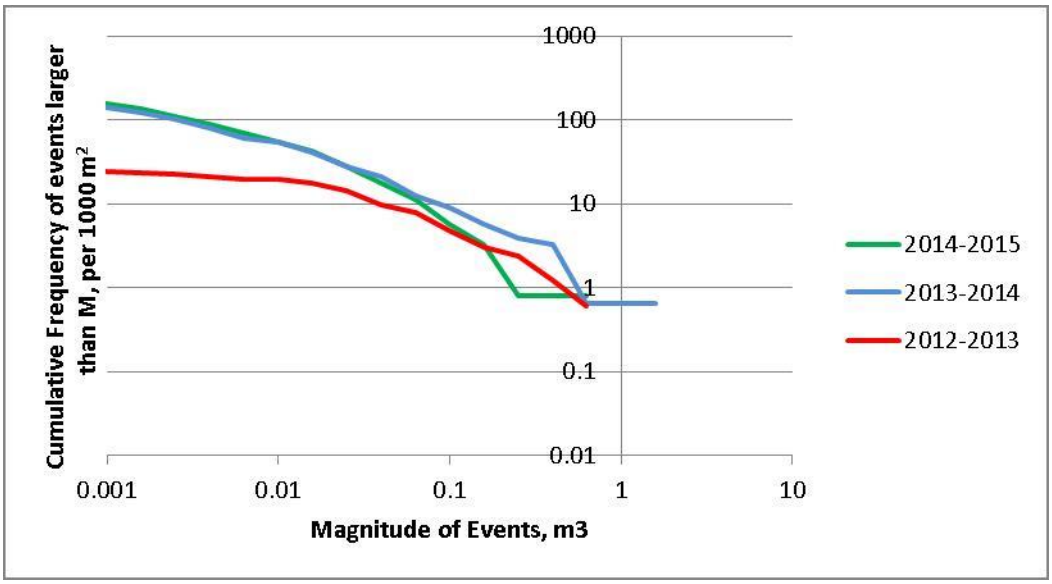

Figure 4.10 Cumulative magnitude–frequency relationships for three approximately 1-year epochs at site LL86.9

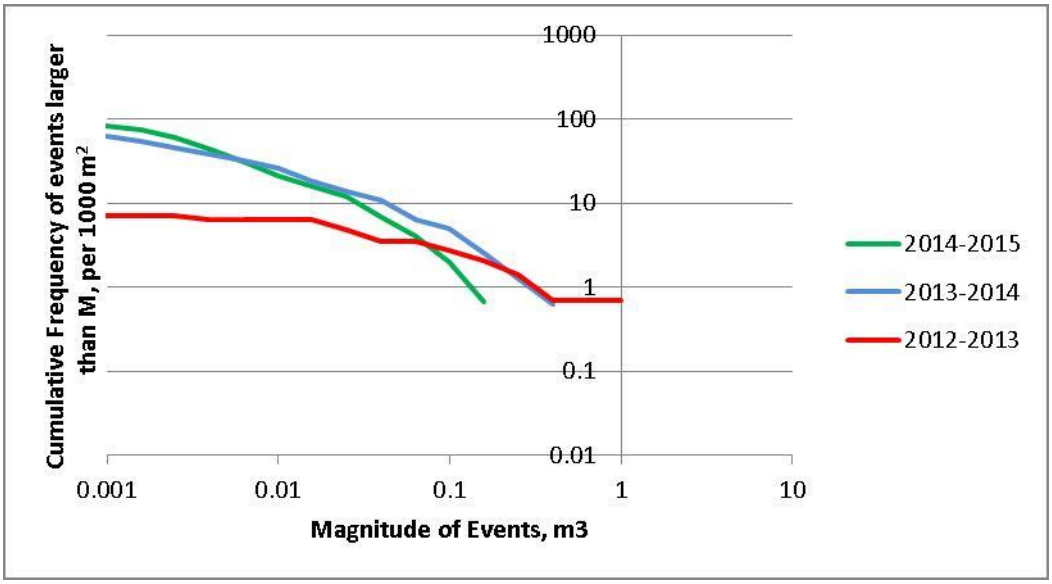

Figure 4.11 Cumulative magnitude–frequency relationships for three approximately 1-year epochs at site LL87

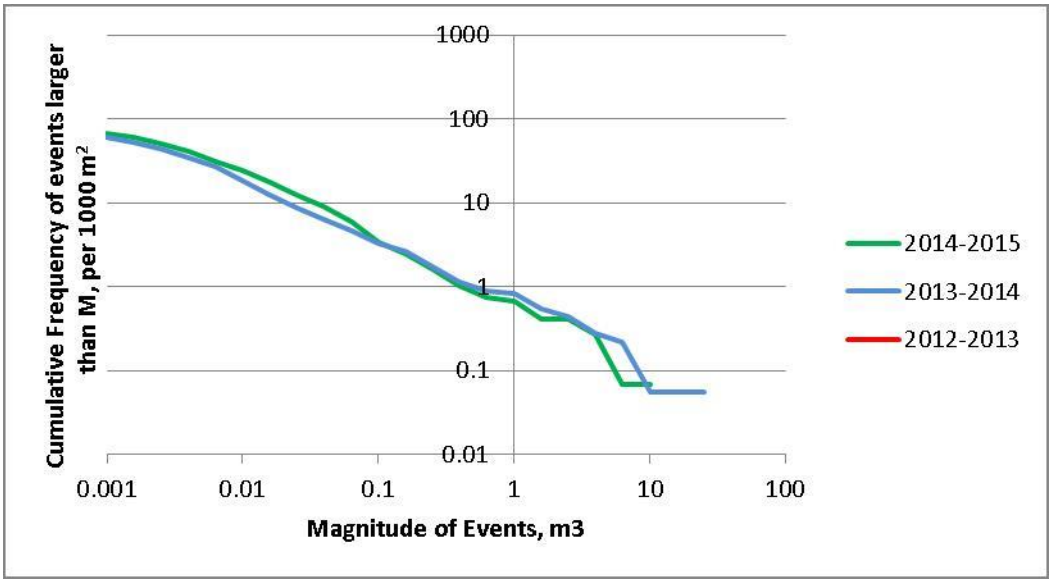

Figure 4.12 Cumulative magnitude–frequency relationships for three approximately 1-year epochs at LL71

4.4 Step 4: Development of a Rockfall Evolution Model

To capture the temporal influence of changing rockslope geometry and various forcing events—climactic, seismic or anthropogenic—a prototypical framework that captures the evolution of rockslopes over time was developed using the same logic as the RAI. This

algorithm, entitled the Rockslope Evolution Framework (REF), incorporates RAI classifications (steep overhangs, talus, etc.) for a given digital terrain model (DTM) discretized as a psuedogrid, assigning a prescribed activity rate (A) and retreat rate (R) to each cell on the basis of its classification at a given time increment t. At time t, each given cell is assigned a random number between 0 and 1 that is representative of the Activity Variable (At). When the Activity Variable falls below a prescribed activity rate for a given cell i at a time increment t (i.e., $A(t) > At(t)$), then the cell will retreat by a distance R(t) normal to the given cell surface. Then, the DTM is reconstructed and its derivatives required for classification (roughness at 35-cm window, R35; roughness at 85-cm window, R85; slope based on surface normal, S) are computed. This new DTM is then used in the next time increment, whereupon all cell classifications are updated on the basis of the new geometry. Concurrent to this, activity rates (A) are updated to account for any type of forcing effects at a given time t—in this preliminary framework, the changes in activity due to increased freeze/thaw cycling. However, the proposed framework maintains the flexibility to incorporate any time-dependent changes in activity that may be derived empirically, including freeze/thaw, precipitation, anthropogenic changes (e.g., blasting, scaling), or seismic forcing. A schematic of the proposed algorithm is presented in figure 4.13.

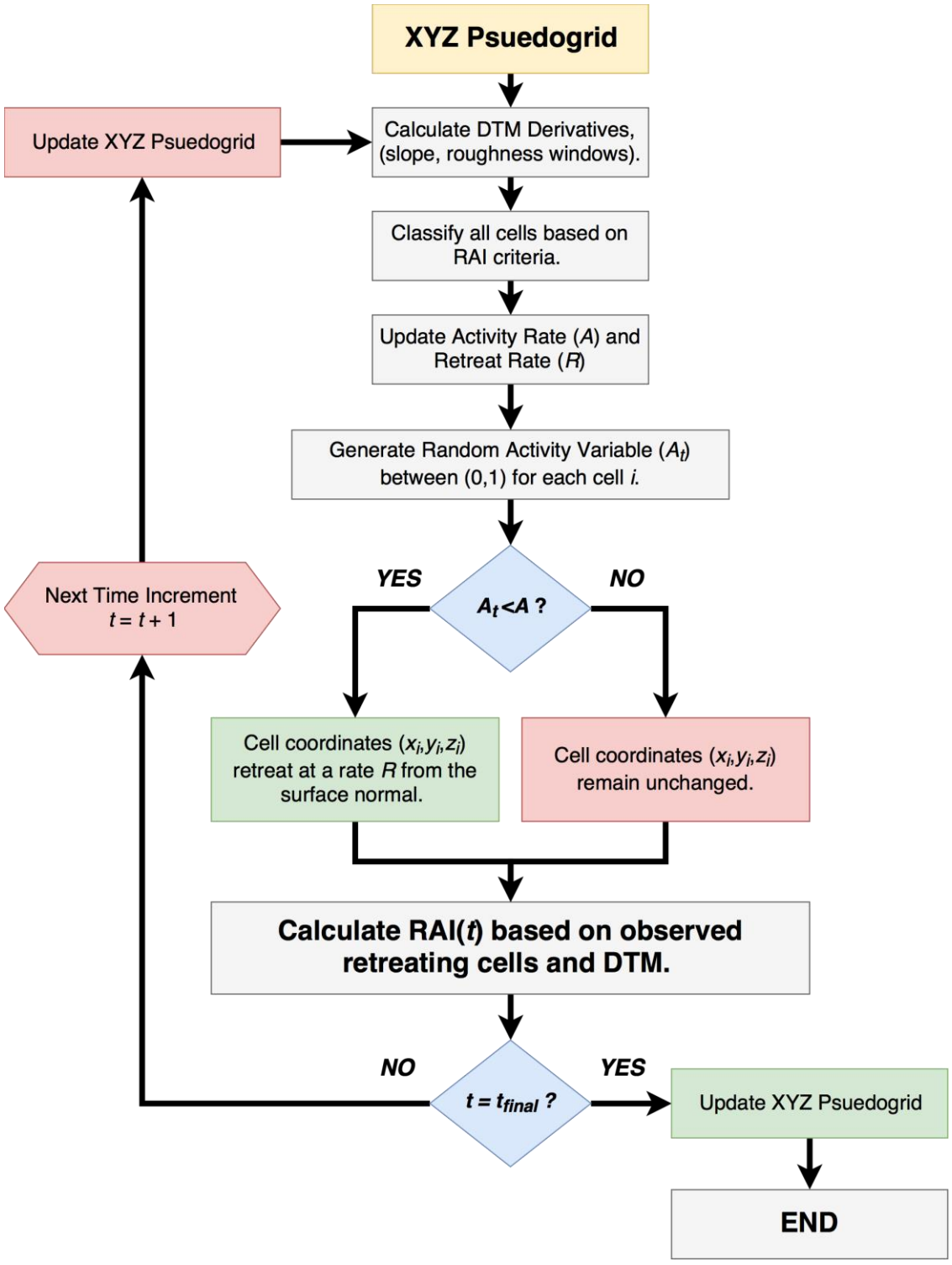

Figure 4.13 Proposed algorithm for implementing the RAI to determine rockfall activity, considering changes in rockslope geometry and activity rates.

The REF was tested on the highly active and well-characterized rockslope located at milepost 88.1 near Long Lake over a 100-year period. For this analysis, the analyzed timestep was 1 year (consistent with the intervals for data collection used to develop the RAI). Every year, the activity rates (A) for the seven classifications (Dw, Dc, Df, I, Oc, Os and T) were assumed to increase at a rate 0.3 percent per year, consistent with increases in average temperatures projected by the Scenarios Network for Alaska + Arctic Planning (SNAP) from 2000 to 2099. The results of the analysis are shown in figure 4.14. It can be seen that the RAI values increase over time along the rockslope profile. The yearly mean RAI showed an increase that is not linear, yet rather exponential, more than doubling over the century-long projections. This implies that the rockfall activity not only increases, but its potential for harm (i.e., clearance between the point of failure on the slope and the roadway) also increases over time. Using changes in climate as an analogue for increased activity, the given increase in A over the 100 years is approximately 35 percent. However, the increase in the mean RAI for the Long Lake site is almost 150 percent, indicating that, hypothetically, small changes in climate may result in much larger changes in rockfall activity and impacts.

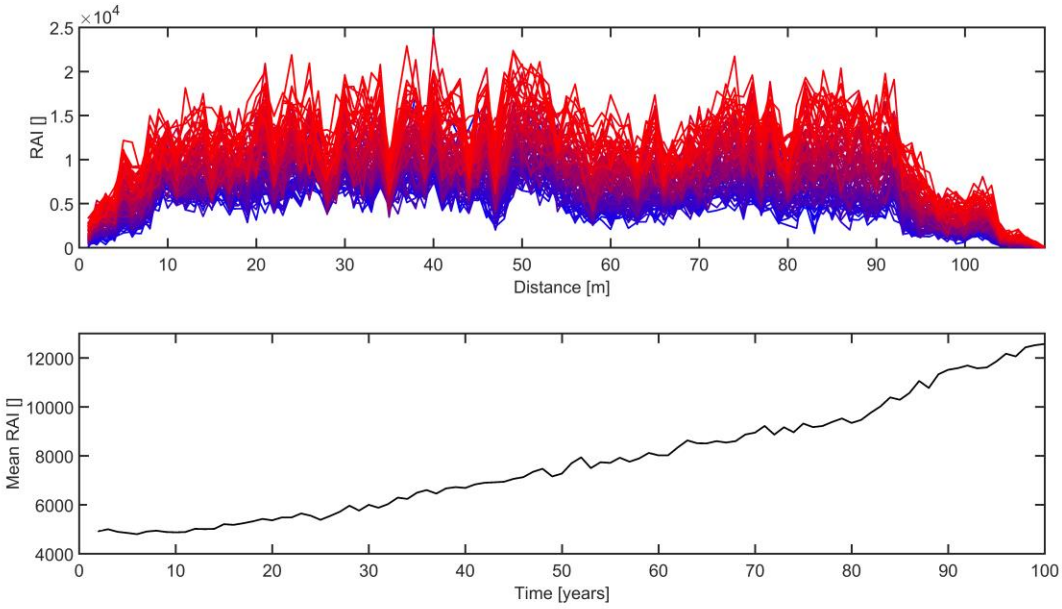

Figure 4.14 Top: Projected evolution of the RAI profile for Long Lake MP 88.1 site over a 100-year period, considering increasing climate influences on established activity rates (blue is current time, red is 100 years from now).
Bottom: Mean projected RAI profile for Long Lake MP 88.1 over a 100-year period. Note that the increasing rockfall activity is not linear.

The 100-year projections from the REF exhibit significant retreat at areas with already high activity and retreat rates (i.e., steep and cantilevered overhangs, figure 4.15 and figure 4.16). Intuitively, these are reasonable findings, as these regions tend to be very exposed and prone to instability due to gravity. Although the given analysis provided profiles after 100 years of rockfall activity (figure 4.16), it is evident that much longer times may result in an eventual transition back to an equilibrated, stable slope. However, within the timespan of engineering structures, the studied rockslopes will remain in an active, unstable state driven by geological structure, slope geometry, and exposure to climactic influences.

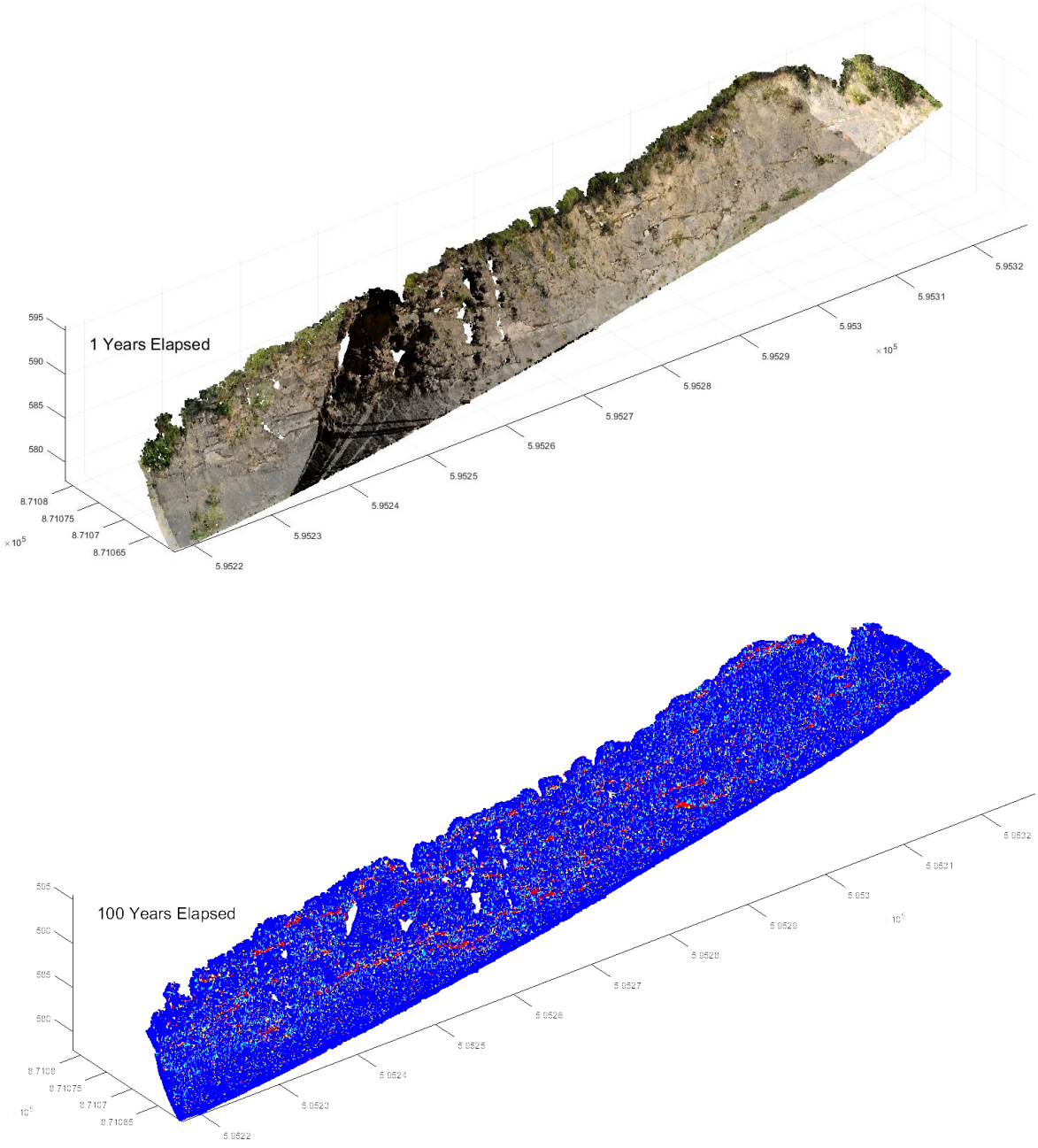

Figure 4.15 Top: Original psuedogrid of RGB 5cm x 5cm cells representative of Long Lake rockslope geometry at the time of data collection.
Bottom: Projected retreat of rockslope after 100 years (red is greater than 2 meters of retreat, blue is no retreat).

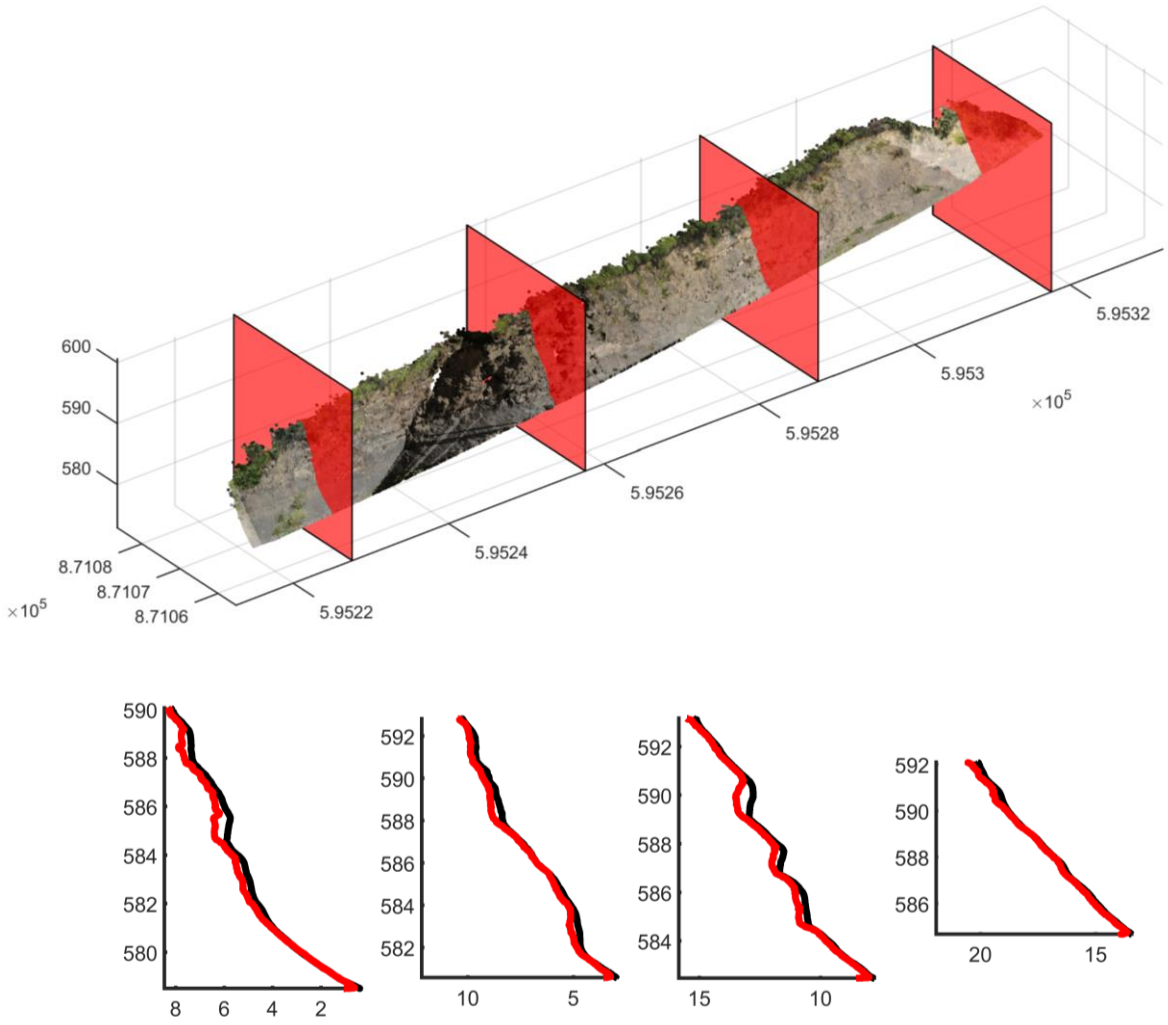

Figure 4.16 Select initial and projected final rockslope profiles along Long Lake site after 100 years of time. Note the rapid retreat of steeper and overhanging sections of weak rock, while a more steady retreat pattern is noted for the more gentle grades.

The proposed REF model uses the RAI methodology to project rockslope changes on the basis of empirically derived activity and retreat rates derived from serial collection of lidar data. This quantification provides a meaningful approach for providing a more resilient infrastructure network. However, the RAI alone does not account for one of the growing threats toward resilience: climate change. Being able to capture the influence of climactic drivers on rockslope

instability quantitatively will enable planners and engineers to prioritize rockfall mitigation measures on the basis of collected empirical data and projected influences. This wil ensure greater resilience today and in the future.

Future modifications will focus on the influence of how these temperatures change freeze/thaw cycling and corresponding activity rates, as the number of freezing and thawing cycles may be used as a proxy for increases in activity for a given year based on climate projections. This work may also account for other climate-forcing influences, including solar radiation (aspect), precipitation, and snow.

4.5 Step 5: Comparison of Slope Change with Historic Weather Patterns

To analyze the historic weather and forecasted climate of the study sites, we first downloaded the historic weather data archived with the National Oceanic and Atmospheric Administration (NOAA). These data for central Alaska dated from 1927, offering 90 years of records to examine. Annual trends resembled weather in many places—a whipsaw of ranges. Nevertheless, the overall trend could be determined. Since 1927, the trend of summer temperatures, as indicated in figure 4.17, has been one of continuous warming.

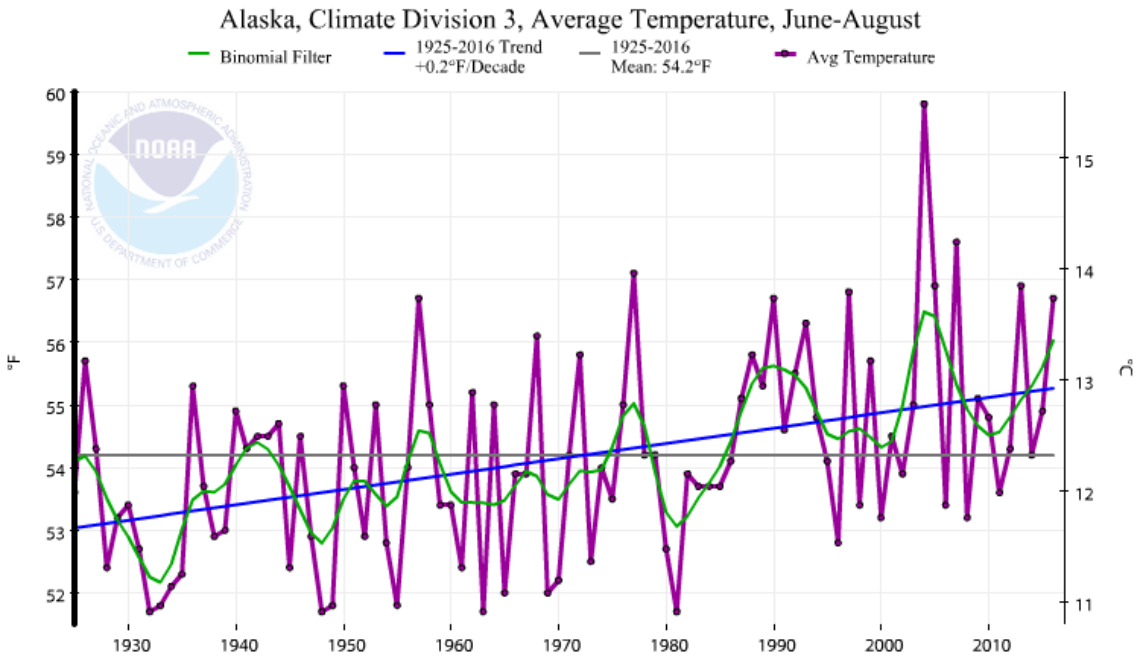

Figure 4.17 Summer temperature warming trend for central Alaska since 1927

Note the horizontal gray line, which is the mean temperature for the entire period of weather observations. The blue line indicates the trend of summer temperatures for July, which depicts a steady increase. During this period, temperatures climbed from an average summer temperature of 55°F to an average of 58°F. The historic data also show that yearly swings in temperature variability skewed with the warming trend.

The same data can be viewed on a differing plot, figure 4.18. In this case, we combined the average summer temperatures for central Alaska, not just for July as in the previous plot, but also for the months of June, July, and August. The warming trend remained the same.

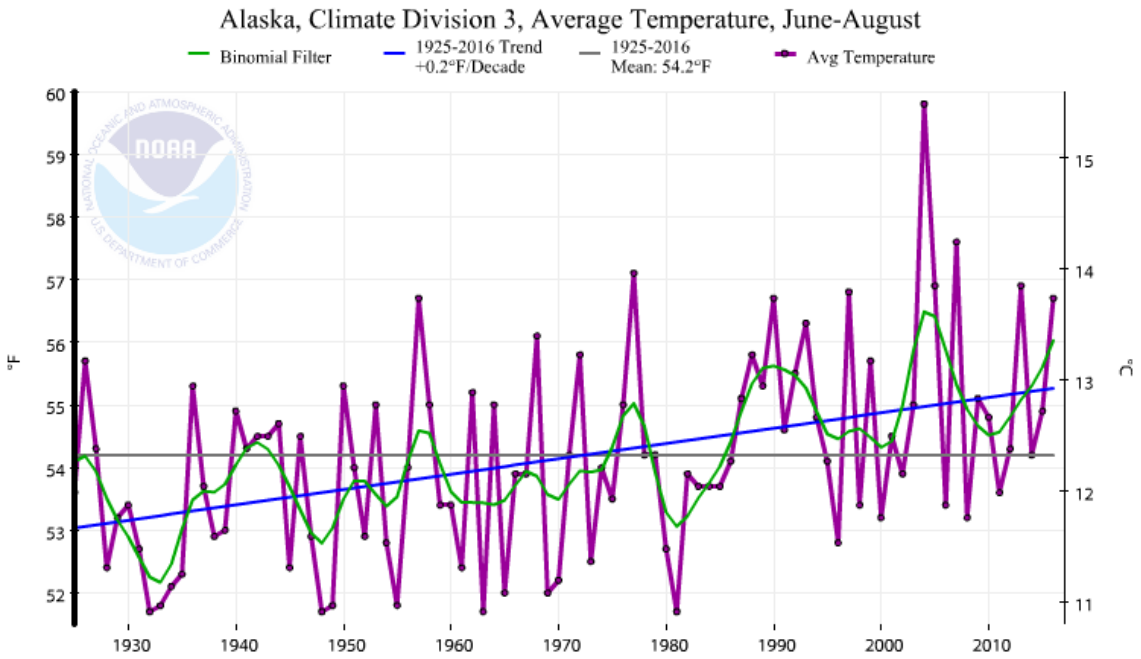

Figure 4.18 Summer temperature warming trend for central Alaska since 1927

There are two additional ways of looking at the temperature trends for central Alaska. The previous two charts provided the average temperatures. When we considered the minimum (figure 4.19) and maximum (figure 4.20) temperatures from June through August, the patterns again remained similar, though the average maximum temperature shifted earlier in the chart.

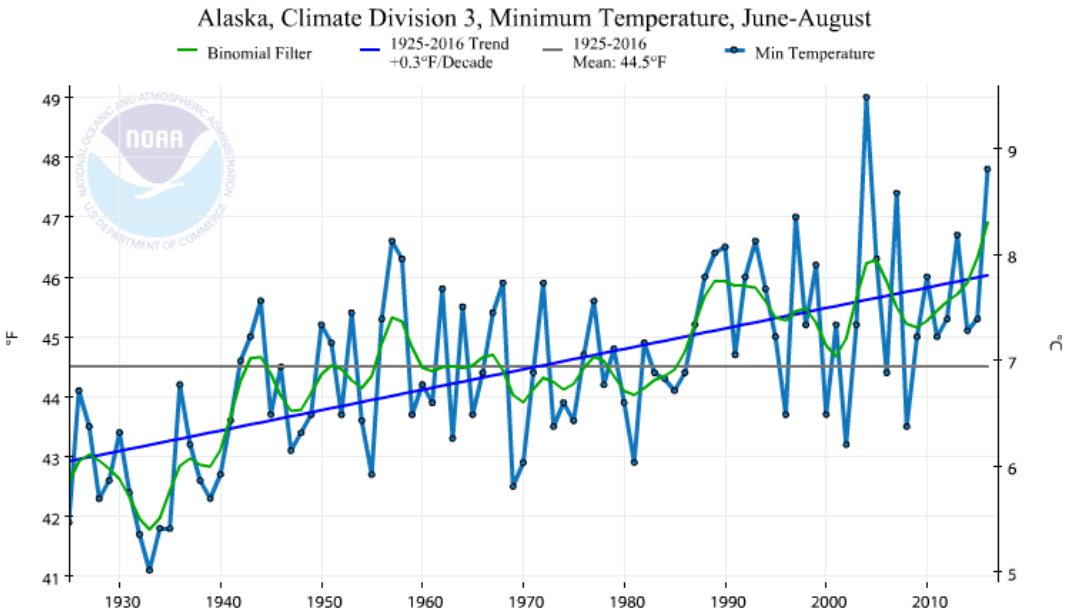

Figure 4.19 Temperature warming trend for central Alaska since 1927 (minimums)

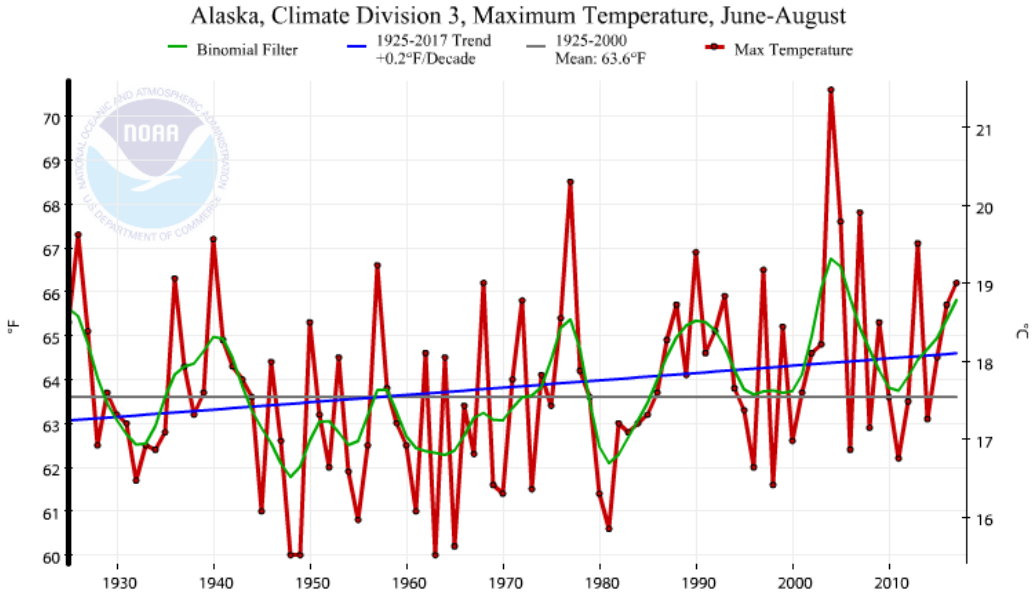

Figure 4.20 Temperature warming trend for central Alaska since 1927 (maximums)

Finally, looking at the historic average temperatures in what is typically the coldest month for central Alaska, February (figure 4.21), the same trend emerged, with a warming trend of about 6°F from 1927 to the present.

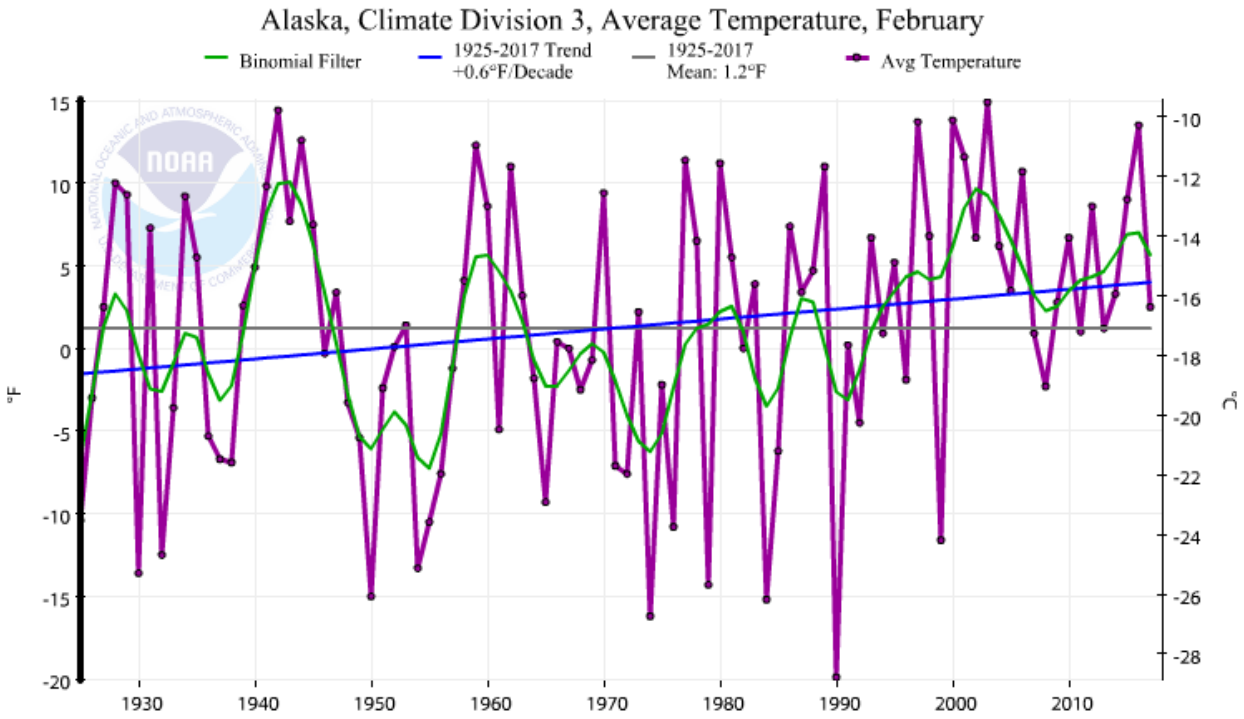

Figure 4.21 Winter temperature warming trend for central Alaska since 1927

The reader is invited to further study these trends at this NOAA link:

https://www.ncdc.noaa.gov/cag/time-series/us/50/3

Chapter 5 Alaska Forecast Models

5.1 Weather Patterns and Climate Forecasts

Climatologists generally refer to weather as the temperature, humidity, and precipitation of a place, typically on a short time scale, such as hour to hour, day to day, and week to week. Climate on the other hand is the weather of a place averaged over a longer time, such as year to year, or over decades. Thus the historic weather data we reviewed provided insight into the changing climate pattern for our study sites.

Climate researchers have noted that Alaska has warmed twice as rapidly as the rest of the U.S. This warming effect is greater in the winter by an average of 6°F, whereas the summers are warmer by 3°F (Chapter 4). Weather variability, with more extremely hot days and fewer extremely cold days, is now the normal pattern affecting transportation corridors in Alaska. The spring snowmelt arrives earlier, glaciers are retreating, and permafrost is thawing longer and deeper during the summers.

A significant warming shift occurred around 1977, when the Pacific Decadal Oscillation (PDO) was observed. The PDO has been shown to alternate over time between cool and warm phases, although the cooler oscillation has been moderated by the long-term warming trend. The PDO is explained by the coupling of warming atmosphere and waters in the eastern Pacific Ocean and is related to El Niño events, among other factors. The oscillations from the PDO pattern can be seen in the previous charts.

The long-term climate patterns in Alaska continue to show a warming trend. Forecast models include variables that are mechanisms that “force” certain patterns. These “forcings” include greenhouse gases, with the greatest influence being carbon dioxide because of its prevalence and link to fossil fuels.

5.2 Climate Forecast Models

The forecast models used to predict monthly average temperatures at our study sites were developed at the University of Alaska Fairbanks by the Scenarios Network for Alaska + Arctic Planning (SNAP). These SNAP models were used to factor a variety of forcings into local, down-scaled forecasts for the specific sites of Long Lake (Chickaloon projection) and Glitter Gulch (Denali Park projection).

The forecast models borrow from models developed by global experts that have been tested for factors associated with Alaska's historic weather patterns. The various models and the scenarios under which they are evaluated lead to differing projections. In the case of the forecasts at our study sites, the greatest variable chosen was that carbon emissions would continue to be released at their current rate.

This current rate of emission is called the "high-range emission," which in effect means that carbon dioxide trends will result in solar energy warming of the Earth's surface at +8.5 watts per square meter. The term RCP 8.5 means representative carbon pathway, which is another forecasting tool specific to several greenhouse gases, not exclusively carbon dioxide forcing.

With the RCP 8.5 assumption, the model showed that average annual temperatures in Alaska are projected to climb steadily for the balance of the 21st century. By 2050 temperatures are expected to grow by an additional 2°F to 4°F above the historic increase from 1927 to 2017. By the end of this century, temperatures in the interior of Alaska are expected to rise 8°F to 10°F.

5.3 Climate Forecasts for Study Sites

The next series of plots are from the SNAP models. The first two charts are temperature projections and variabilities at Chickaloon (Long Lake, figure 5.1 and Denali Park (Glitter

Gulch, figure 5.2). Note that the historic data are in the first two bars (gray and light orange), whereas the longer-range forecasts are displayed the darker orange colors. Superimposed on each bar is the variability of the projection (from the normal statistical distribution), which provides an estimate of how the daily temperatures (weather) may vary within the overall climatic pattern.

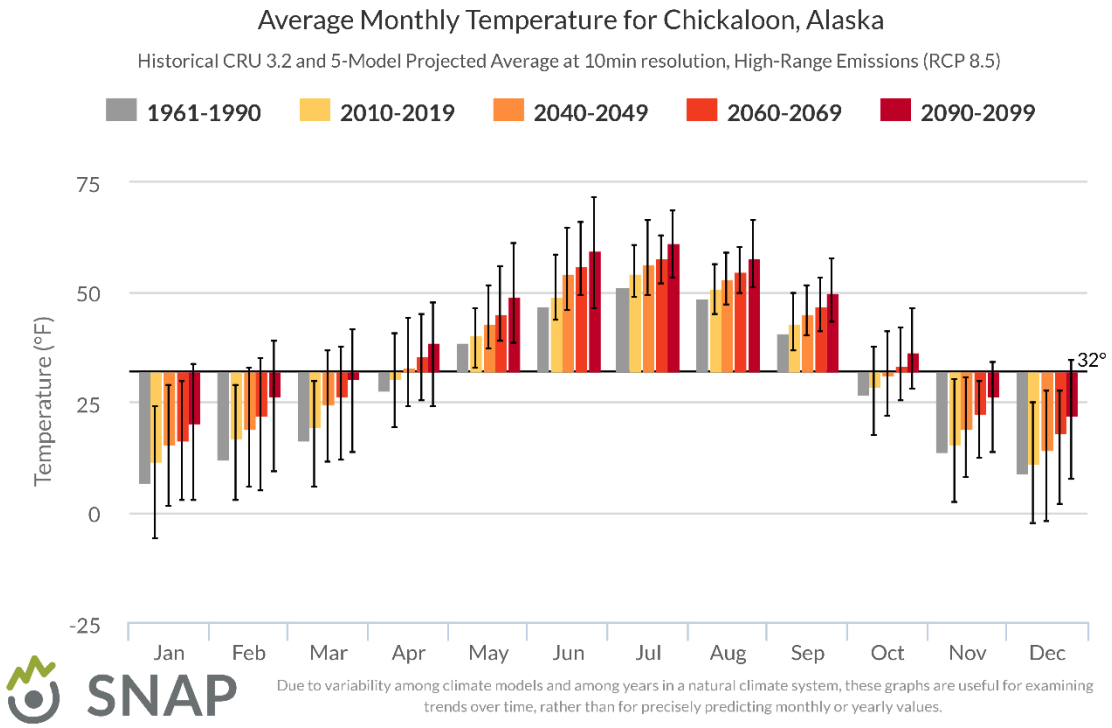

Figure 5.1 Temperature forecast at Long Lake through 2099

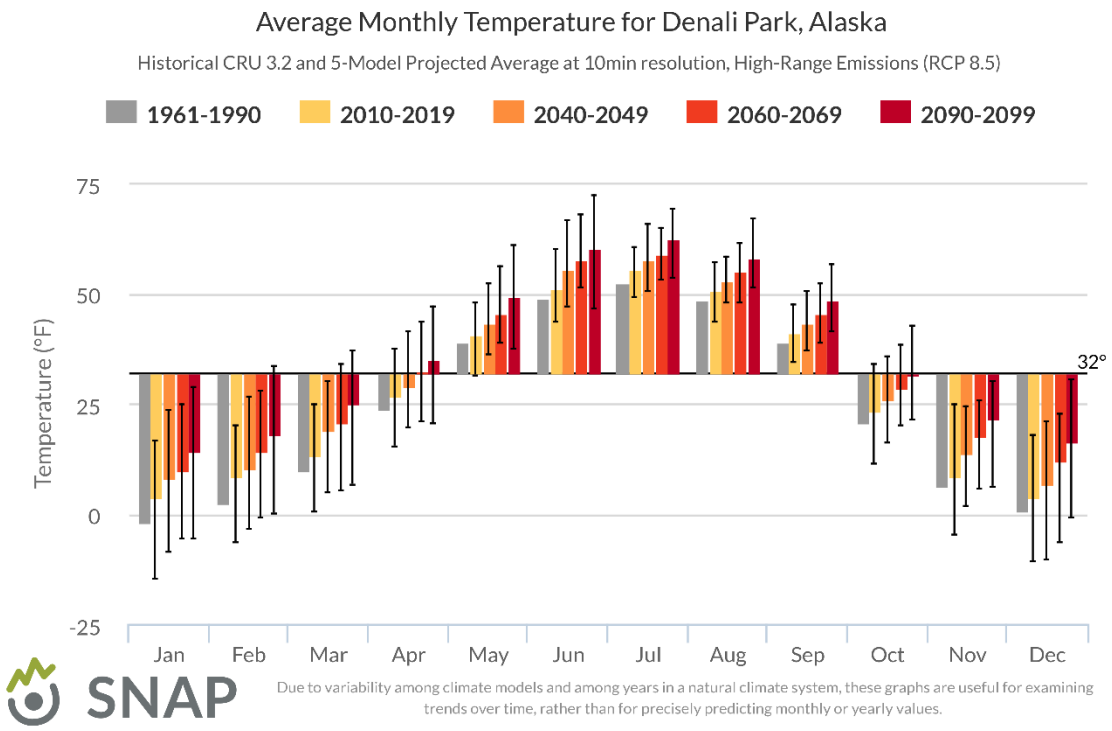

Figure 5.2 Temperature forecast at Glitter Gulch through 2099

The same forecasting models were also used to estimate the precipitation at each study site. The following two charts (figures 5.3 and 5.4) for the study sites show increasing precipitation and a profoundly varying range of precipitation events, which are correlated to climate change, in general.

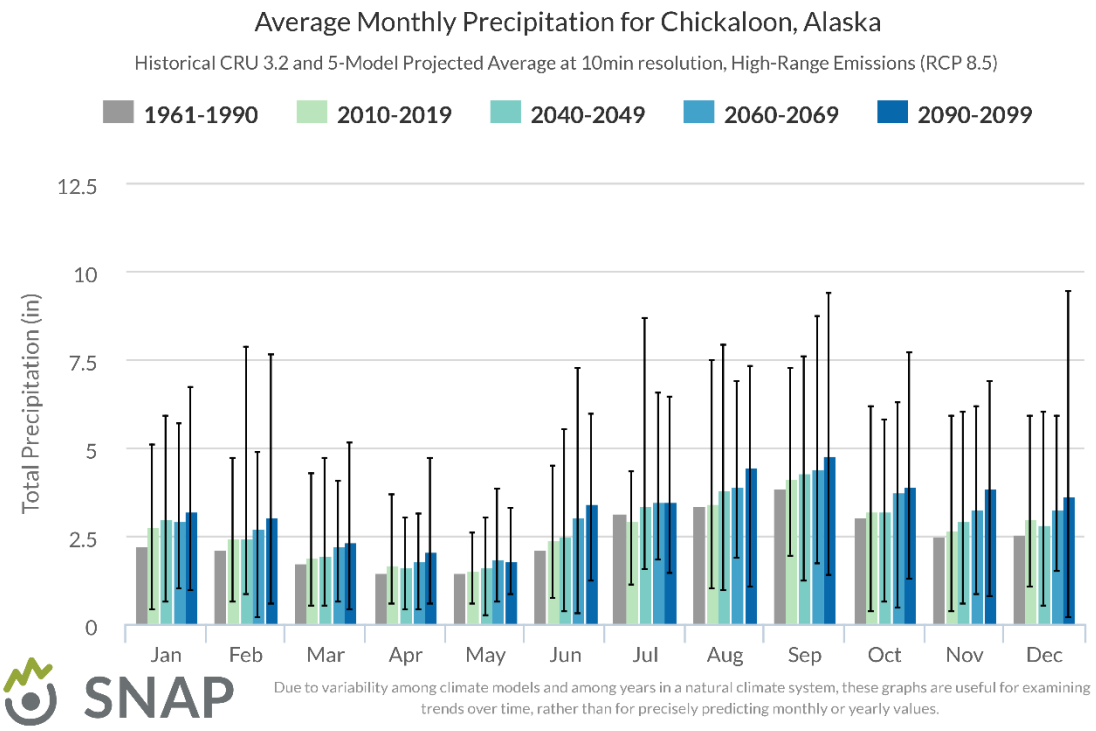

Figure 5.3 Precipitation forecast at Long Lake through 2099

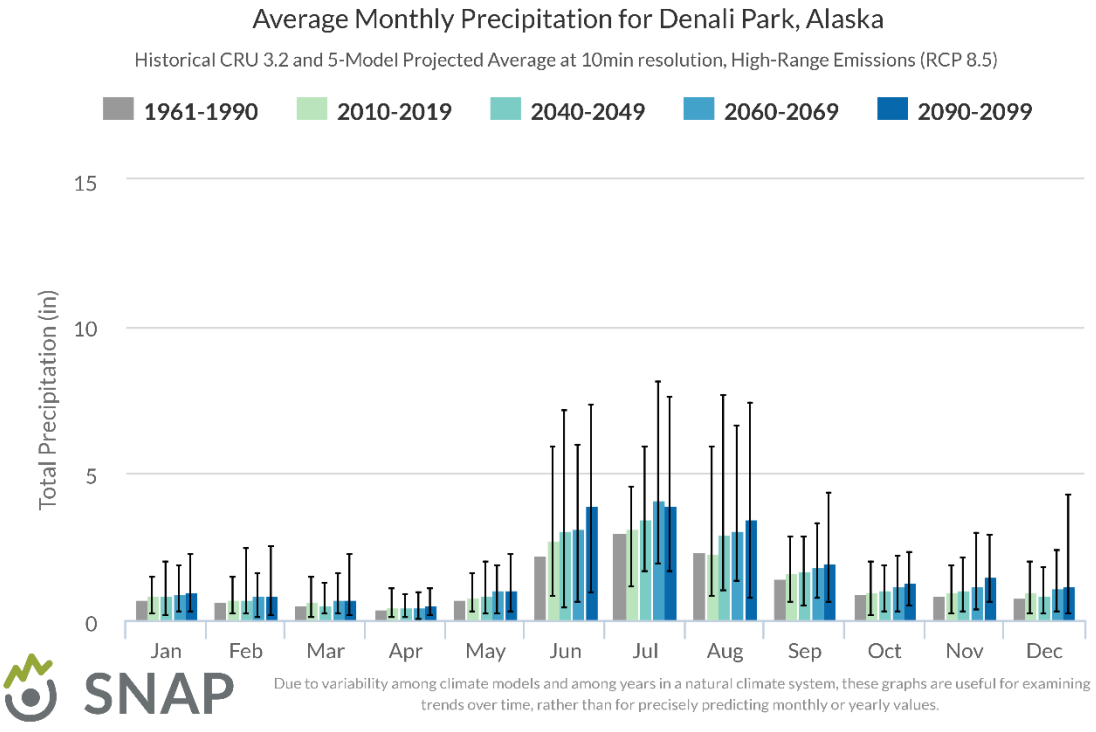

Figure 5.4 Temperature forecast at Glitter Gulch through 2099

Chapter 6 Conclusions and Recommendations

This Phase IV research project attempted to understand the quantitative slope changes the team has measured since 2012 at Long Lake and Glitter Gulch, Alaska, with historic weather data and forecasted climate trends. A quantitative framework called the RAI provided a reliable way to assess rockfall activity and the impacts of these geohazards using a serial collection of rockfall data. The RAI is versatile tool that enables users to collect rockfall activity and prioritize mitigation measures within a data-driven, engineering-based framework. Such a measure is important for assessing the resilience of our infrastructure *today*.

To capture the influence of climate change on rockfall activity, the progressive failures observed in rockslopes must be quantified and projected by using a rational, data-driven engineering approach. The change in rock slope morphology at the study sites showed continuous rockfall, talus accumulation, and overall progressive mass wasting. It is understood that rockfall events may be tied to freeze/thaw cycling and heavy precipitation, suggesting that the influence of a changing climate is important to future rockfall activity. Although our quantitative baseline for our slope study sites was limited to five years, this data set provides invaluable information regarding prolonged rockfall activity, which is essential for assessing the long-term impacts of a changing climate. The key to understanding a correlation with the dynamics of our study sites in the face of a changing climate will be to use our baseline measurements with new digital terrain models (DTMs) (via terrain laser scanning and and structure from motion scanning). Facing limited research budgets and changing priorities, the team suggests collecting new DTM data approximately every five-or-so years to continue this analysis while capturing the variability observed in yearly weather. The repeated surveys can then be used to formulate better mitigation strategies for the rockfall patterns observed, as well as

to develop mitigation budgets. Thus, a data-driven approach based on the collected data is paramount to the safety and resilience of critical transportation corridors *today and in the future*.

On the basis of the collected serial data and the Rockfall Activity Index (RAI) approach, a framework for assessing projected rockslope activity based on changes in time-dependent classification and DTM evolution was developed, entitled the *Rockslope Evolution Framework* (REF). This prototype was used to project the potential impacts of a changing climate, in this case using temperature increase as a proxy for increasing rockfall activity. The results showed that the yearly RAI for a given site may increase significantly more than the observed activity rate. **That is, the slow and gradual increase of activity due to climate change may result in significant increases in rockfall impacts—a direct threat to the safety and resilience of critical corridors.** In light of this possibility, creating more resilient critical infrastructure will require adaptation of planning tools to address rockfall today (the RAI) and in the future (the REF). By considering the looming threats of climate change, we enable planners and engineers to make data-driven solutions for a more resilient *future*.

There is a lot of uncertainty in predicting climate change that far into the future given that policies, technology, habits, lifestyles, and priorities will all continue to evolve. Nevertheless, a longer-term perspective and monitoring campaign could create more definitive connections between the individual weather events that are part of climate change and the dynamics of rockfall and slope stability. Each perspective is important to further risk assessment, and mitigation planning with forecasting models can also be used to estimate the precipitation at each study site. Note that the two charts provided for the study sites showed increasing precipitation and a profoundly varying range of precipitation events, which are correlated to climate change, in general.

References

Badger, T.C. and Lowell, S. 1992. Rockfall Control Washington State. In Rockfall Prediction and Control and Landslide Case Histories, Transportation Research Record, National Research Council, Washington, No 1342, 14-19.

Barlow, J., Lim, M., Rosser, N., Petley, D., Brain, M., Norman, E., Geer, M. (2012) Modeling cliff erosion using negative power law scaling of rockfalls, Geomorphology, Volumes 139–140, 15 February 2012, Pages 416–424.

Bedford and Cooke. 2001. Probabilistic Risk Analysis: Foundations and Methods. Tim Bedford and Roger Cooke. Cambridge University Press. Cambridge, United Kingdom.

Budetta P, Nappi, M (2013) Comparison between qualitative rockfall risk rating systems for a road affected by high traffic intensity, Nat. Hazards Earth Syst. Sci., 13:1643-1653, doi:10.5194/nhess-13-1643-2013

Burns, W. J., & Madin, I. (2009). Protocol for inventory mapping of landslide deposits from light detection and ranging (LiDAR) imagery. Oregon Department of Geology and Mineral Industries.

Connor, B. and Harper, J. (2013). How Vulnerable Is Alaska's Transportation to Climate Change? Managing an Infrastructure Built on Permafrost.

Cunningham, K., Olsen, M., Wartman, J. http://depts.washington.edu/pactrans/wpcontent/uploads/2013/11/PacTrans_42-UAF-Cunningham.pdf

Dunham, L., Wartman, J., Olsen, M.J., O'Banion, M.S, & Cunningham, K. (2017). "Rockfall Activity Index (RAI): A Lidar-derived, morphology-based hazard assessment system," Engineering Geology, 221, 184-192. https://doi.org/10.1016/j.enggeo.2017.03.009

FHWA (2016) Geohazards, Climate Change, and Extreme Weather Events – Synthesis Report.

Hicks, D.L., 1995. A way to estimate the frequency of rainfall-induced mass movement. Journal of Hydrology (New Zealand) 33 (1), 59–67.

Larsen, P.H., et al., Estimating future costs for Alaska public infrastructure at risk from climate change. Global Environmental Change (2008), doi: 10.1016/j.gloenvcha.2008.03.005

Metzger, A., Olsen, M., Cunnigham,K. http://depts.washington.edu/pactrans/wpcontent/uploads/2012/12/PacTrans-2-739439-Metzger-Andrew-Multi-Project.pdf

Nat. Acad. of Sci. (2016), Attribution of Extreme Weather Events in the Context of Climate Change

National Climate Assessment (2016). Retrieved July 06, 2016, from http://nca2014.globalchange.gov/highlights/regions/alaska.

Nicolson, Dawn T. 2004. “Introduction to the RDA (Rockslope Deterioration Assessment”. Publshed at: http://www.dawntnicholson.org.uk/. Accessed 10/9/2013

O’Banion, M.S.*, Olsen, M.J., Rault, C., Wartman, J., and Cunningham, K. (Accepted). “Suitability of Structure from Motion for Rock Slope Assessment,” submitted to the Photogrammetric Record.

Occhiena, C., and Pirulli, M. (2012), "Analysis of Climatic Influences on Slope Microseismic Activity and Rockfalls: Case Study of the Matternhorn Peak (Northwestern Alps)," Journal of Geotechnical and Geoenvironmental Engineering, American Society of Civil Engineers, vol. 138, issue 8, pp. 1012-1021.

Olsen, M.J., Wartman, J., McAlister, M., Mahmoudabadhi, H., O’Banion, M.S., Dunham, L., and Cunningham, K., (2015). “To fill or not to fill: Sensitivity analysis of the influence of resolution and hole filling on point cloud surface modeling and individual rockfall event detection.” Remote Sensing, Special Issue- Use of lidar and 3D point clouds in geohazards, 79(9),12103-12134. doi:10.3390/rs70912103

Palmstrom, A. (1995). RMi - A system for characterizing rock mass strength for use in rock engineering. *Journal of Rock Mechanics and Tunneling Technology, 1(2)*, 69-108.

Pierson, L. A. (1991). Rockfall Hazard Rating System. Washington, DC: Federal Highway Administration.

Scott, P. (2016) How climate change affects extreme weather events, Science, 352, p. 1517

Washington DNR. Landslides | WA - DNR. (2016). Retrieved July 06, 2016, from http://www.dnr.wa.gov/programs-and-services/geology/geologic-hazards/landslides.

Bibliography

Alaska Dispatch News (2016) Rock climbers put their skills to work improving highway safety near Denali Park, http://www.adn.com/business-economy/energy/2016/06/25/denali-climbers-chip-away-at-crumbling-rock-walls-as-summer-traffic-flows-by-100-feet-below/

Jaboyedoff, M., Oppikofer, T, Abellan, A., Derron, M.H., Loye, A., Metzger, R., Pedrazzini, A. 2010."Use of LiDAR in landslide investigations: a review," *Natural Hazards*.

Kemeny, J., and Turner, A.K., (2008) "Ground-based LiDAR Rock slope mapping and assessment," Publication No. FHWA-CFL/TD-08-006.

Kemeny, J., Norton, B., Handy, J., and Donovan, J. (2008). "Three-dimensional digital imaging for the identification, evaluation and management of unstable highway slopes," Final Report for Highway IDEA project 119, TRB NAS.

Mohamed, K. (2016). "Geohazards, Climate Change, And Extreme Weather Events—Peer Exchange Report."

Nicolson, Dawn T. 2005a. "RDA Stage One". Published at: http://www.dawntnicholson.org.uk/. Accessed 10/9/2013

Nicolson, Dawn T. 2005b. "Hazard assessment for progressive, weathering-related breakdown of excavated rockslopes." Quarterly Journal of Engineering Geology and Hydrogeology, 37, 327–346.

Olsen, M.J.; Johnstone, E.; Driscoll, N.; Ashford, S.A.; Kuester, F. Terrestrial laser scanning of extended cliff sections in dynamic environments: Parameter analysis. *J. Surv. Eng.* 2009, *135*, 161–169.

Olsen, M.J., 2013. In Situ Change Analysis and Monitoring through Terrestrial Laser Scanning. Journal of Computing in Civil Engineering, 29(2).

Olsen, M.J.; Roe, G.V.; Glennie, C.; Persi, F.; Reedy, M.; Hurwitz, D.; Williams, K.; Tuss, H.; Squellati, A.; Knodler, M. *Guidelines for the Use of Mobile LiDAR in Transportation Applications*; TRB NCHRP Final Report 748; Publisher: TRB Washington, DC, USA, 2013.

SNAP (2016) Dynamical downscaling techniques yield new understandings and attention, https://csc.alaska.edu/research-highlights/dynamical-downscaling-techniques-yield-new-understandings-and-attention

Vessely, M. (2013). "Risk-based methods for management of geotechnical features in transportation infrastructure," Proc. ASCE GeoCongress 2013.

Wahrhaftig, Clyde, and Robert F. Black. "Engineering Geology along part of the Alaska Railroad." Geological Survey Professional Paper 293, 1958: 71-116.

Western Regional Climate Center, Last Visited November 30, 2013, http://www.wrcc.dri.edu/summary/Climsmak.html.

Appendix A

Manuscript Draft

Accepted for Publication in *The Photogrammetric Record*

Suitability of structure from motion for rock-slope assessment

O'Banion, M.S., Olsen, M.J., Rault, C., Wartman, J., and Cunningham, K.

Abstract

This study examines three sites with unstable rock-slopes that were surveyed in Alaska using both TLS and SfM techniques. The datasets were acquired simultaneously and linked to a rigorous survey control network. An accuracy evaluation of the SfM-derived surface models was performed using TLS data and numerous reflectorless total station observations collected across the rock-slopes. A quality evaluation was conducted to examine differences in point density, model completeness, and distributions of morphological properties between the SfM and TLS datasets. The results indicate that SfM is a viable option for unstable rock-slope assessment when a sufficient quantity of images with adequate overlap are acquired, and the reconstruction is tied to a survey control network. The best results in terms of accuracy and completeness were achieved when combining both UAS-based aerial imagery and terrestrial imagery for the SfM reconstruction. However, artifacts observed in the SfM data, such as over-smoothing and geometric inconsistencies bring into question the suitability of SfM for detection of small changes over time.

Keywords: rock-slopes, structure from motion (SfM), accuracy assessment, lidar, terrestrial laser scanning (TLS), unmanned aircraft systems (UAS)

Introduction

Terrestrial laser scanning (TLS), also known as terrestrial or ground-based lidar, has proven to be a valuable, reliable technique for the assessment and monitoring of unstable slopes; however, even with numerous setups, portions of a slope or cliff may not be visible from areas accessible to the scanner, resulting in the inability to capture important features of the slope morphology. In lieu of TLS, unmanned aircraft systems (UAS) and a

handheld camera may gather overlapping digital imagery to generate similar three-dimensional (3D) point clouds by way of Structure from Motion (SfM) and multi-view stereo (MVS) photogrammetric techniques (hereafter collectively referred to as SfM). Use of UAS can provide superior accessibility to cliffs and the acquisition of cliff geometry compared to TLS methods.

This study examines three unstable road cuts along the Glenn Highway in Alaska, U.S.A. with different morphologies to evaluate the suitability of SfM for rock-slope assessment. SfM suitability is judged relative to TLS methods with regards to absolute accuracy (i.e., including geo-referencing error) and quality of the 3D data. While previous studies have attempted to assess the accuracy of SfM-based image reconstructions (e.g., Harwin and Lucieer, 2012; James and Robson, 2012; Eltner et al., 2016; Westoby et al., 2012; Fonstad et al., 2013; Lato et al., 2015; James et al., 2017a; James et al., 2017b), they commonly use a single, independent reference consisting of airborne or terrestrial lidar. In many of these cases, no accuracy assessment of the lidar-based reference is performed or documented. This study presents an accuracy assessment that is both rigorous and comprehensive. Two independent references are used for the accuracy assessment: co-acquired TLS data and a collection of reflectorless total station (TS) points collected across the surface of the rock-slopes. The rock-slope TS points serve to evaluate the accuracy of the TLS data, ensuring it is appropriate for judging the accuracy of the SfM data. The rock-slope TS points also serve as a second reference for judging the accuracy of the SfM data. Occasionally, studies will report accuracies of SfM models that simply represent geo-referencing residuals from surveyed ground control points (GCPs) or based on discrepancies with surveyed checkpoints. When surveyed checkpoints are visible in the imagery as high contrast targets (e.g., Harwin and Lucieer, 2012; Fassi et al., 2013), the accuracy assessment can be overly optimistic. The performance of a SfM algorithm when automatically identifying key features in overlapping imagery is directly correlated to the presence of high contrast, textural differences in photographs. Employing highly visible, high contrast GCPs, therefore, results in evaluating accuracy at locations where SfM is theoretically performing at its best (Javadnejad and Gillins, 2016). The independent references used for this study were chosen to evaluate the accuracy throughout the majority of the SfM reconstruction.

This paper presents an evaluation of the suitability of SfM for rock-slope assessment. Accuracy is analyzed through a comparison with two high-accuracy, high precision independent references, tied to a rigorous survey control network. In addition, a quality assessment of SfM data relative to TLS examines important factors such as point density, surface model completeness, and surface morphology. These additional quality metrics have not been

thoroughly or formally evaluated in prior work, which has focused primarily on geometric accuracy. In the context of the accuracy and quality evaluations, comparisons were performed between ground and UAS-based SfM models, as well as, combination SfM (Combo SfM) models in which both ground and UAS-imagery was utilized.

Background

Road cuts through rocky terrain often result in steep rock-slopes, which can be susceptible to rockfall – a process involving detachment, fall, rolling, and bouncing of rocks (Hungr et al., 2014). Rockfall is a reoccurring hazard along transportation corridors in mountainous regions throughout North America. Tens of millions of dollars ($US) are spent annually on rock-slope maintenance and mitigation (Turner and Jayaprakash, 2013).

Current methods for characterization of rockfall hazards and risk rely on rock mass classification (e.g., Pantelidis, 2009) or rockfall hazard rating systems (e.g., Pierson, 2013) that depend on manual visual inspection and simplified calculations. These methods are both qualitative in nature (Budetta and Nappi, 2013) and coarse in spatial resolution. TLS allows for systematic acquisition of rock-slope 3D geometry at high, cm-scale spatial resolutions (Jaboyedoff et al., 2012; Abellán et al., 2014). TLS has been proven as an appropriate method for rock-slope characterization (Jaboyedoff et al., 2012; Abellán et al., 2009; Abellán et al., 2010; Abellán et al., 2014; Alba et al., 2009; Alba and Scaioni, 2010; Kemeny and Turner, 2008; Rabatel et al., 2008; Girardeau-Montaut, 2017; Kromer et al., 2015; Gigli and Casagli, 2011), and monitoring (Lim et al., 2005; Lim et al., 2010; Rosser et al., 2005; Rosser et al., 2007; Lato et al., 2009; Olsen et al., 2009; Olsen, 2013).

TLS offers advantages in terms of accuracy, repeatability, and reliability; however, challenges exist such as cost and the common occurrence of occlusions. SfM-based image reconstruction has the potential to solve these challenges (Fonstad et al., 2013; Chandler and Buckley, 2016). Acquisition of imagery for SfM reconstruction using a UAS offers further advantages in terms of terrain accessibility (e.g., Lato et al., 2015). UAS imagery acquisition and subsequent SfM model reconstruction have proven useful for landslide analysis and digital rock outcrop acquisition. Researchers have utilized repeat surveys from UAS platforms to quantify landslide displacements of large, slow-moving landslides (Niethammer et al., 2012; Fernández et al., 2015; Fernández et al., 2016; Lucieer et al., 2014; Turner et al., 2015). Others have utilized the imagery for mapping landslide features such as scarps and deposits for small areas (e.g., Al-Rawabdeh et al., 2016). For example, Murphy et al. (2016) utilized UAS to map damages from the 2014 Oso landslide in Washington, and Greenwood et al. (2016) utilized UAS to map rock

masses and slides in Nepal after the 2015 earthquake event. Lastly, Manousakis et al. (2016) utilized UAS SfM for rockfall hazard analysis. SfM-based digital outcrop acquisition has been successfully performed by various studies (e.g., James and Robson, 2012; Bemis et al., 2014; Lato et al., 2015a; Wilkinson et al., 2016). However, results of a comparison with co-acquired TLS data from Wilkinson et al. (2016) indicates that the precision of SfM data can deteriorate near the outcrop edges and over-smoothing rounds off sharp rock edges within the outcrop. It is also worth noting that Wilkinson et al. (2016) states that an "elaborate" data acquisition and processing approach is often required to achieve results similar to TLS.

Eltner et al. (2016) present an extensive review of SfM accuracies reported by 39 different published geoscientific studies. The following factors introduce error into SfM-based 3D reconstructions: the scale of the object/environment being captured, the distance of the camera from the imaged object(s), camera calibration, image network geometry, image-matching performance, surface texture and lighting conditions, and GCP characteristics (Eltner et al., 2016). In terms of accuracy of SfM, Eltner et al. (2016) report no significant issues that cannot be mitigated by placement of GCPs, camera calibration or a high number of images. This is true with the exception to having a lack of textural detail in the imaged scene. Homogeneous surface texture commonly prevents automated feature matching algorithms from resolving coincident points and generating accurate 3D geometry (Bemis et al., 2014). Nevertheless, many aspects of image acquisition, GCP network design, and subsequent SfM processing vary substantially study to study. These ad-hoc approaches result in difficulties when attempting to systematically compare accuracies reported by numerous studies (Eltner et al., 2016; James et al., 2017a), and when reporting accuracies of a given SfM collection based on previously achieved accuracies. These disparities are partly due to unknowns with regards to performance and uncertainty associated with image feature matching utilized by SfM algorithms (Eltner et al., 2016), some of which are proprietary (e.g., Agisoft Photoscan). It is for this reason that the use of a trusted independent reference such as TLS is needed to appropriately judge the accuracy of SfM under the unique conditions and methods followed for a given study.

Study Area

The study area is located approximately 110 km northeast of Anchorage, Alaska, U.S.A. along the Glenn Highway (Fig. 1). The region is primarily comprised of sedimentary rocks of the Matanuska and Chickaloon Formations. The Matanuska Formation is a marine sedimentary deposit formed during the orogenic rise of the

Talkeetna Mountains. The Chickaloon Formation was deposited as propagating alluvial fans on top of the Matanuska Formation that formed as the Talkeetna Mountains were uplifted and sequentially eroded (Belowich, 2006). The highway follows the glacial cut into the Chickaloon Formation; however, no other glacial evidence may be found in the area (Trop et al., 2015). Regions of the Matanuska Formation exposed in road cuts along the Glenn Highway largely consist of dark mudstones while Chickaloon Formation outcrops mainly consist of carbonaceous siltstone, coal, and sandstone (Trop et al., 2015).

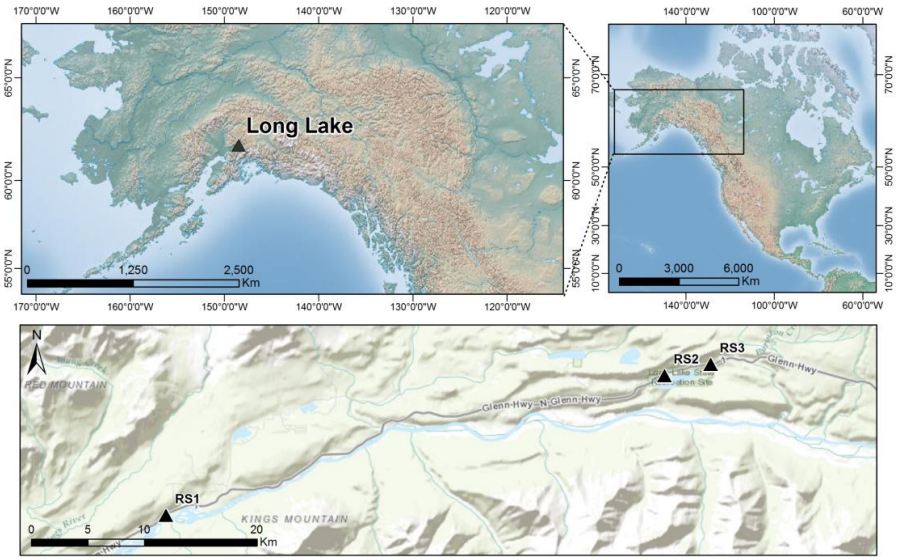

Fig. 1. Study area location plan. Three independent sites were selected: RS1, RS2, and RS3. Basemap imagery was provided by ESRI ArcGIS Online.

Three independent sites were selected for this study (Fig. 2). Rock-Slope 1 (RS1, milepost 71) is a nearly vertical (70° to 90°) road cut approximately 50 to 60 m high and 140 m wide. RS1 is composed of well-indurated dark mudstone of the Matanuska Formation. Rock-Slope 2 (RS2, milepost 85.5) is a 60° road cut approximately 8-10 m high and 40 m wide. RS2 consists of highly fractured, fine to medium-grained, moderately weathered grey and tan hard sandstone of the Chickaloon Formation. The fractures are oriented such that the sandstone is broken into cobble-sized blocks. Rock-Slope 3 (RS3, milepost 87) is a 55° slope approximately 10 m high and 110 m wide. RS3 is predominantly comprised of soft carbonaceous siltstone of the Chickaloon Formation that has been intruded by

hard, well-indurated mafic basalt sills. Numerous cantilever overhangs exist on RS3 because of localized erosion of the soft siltstone beneath the sills.

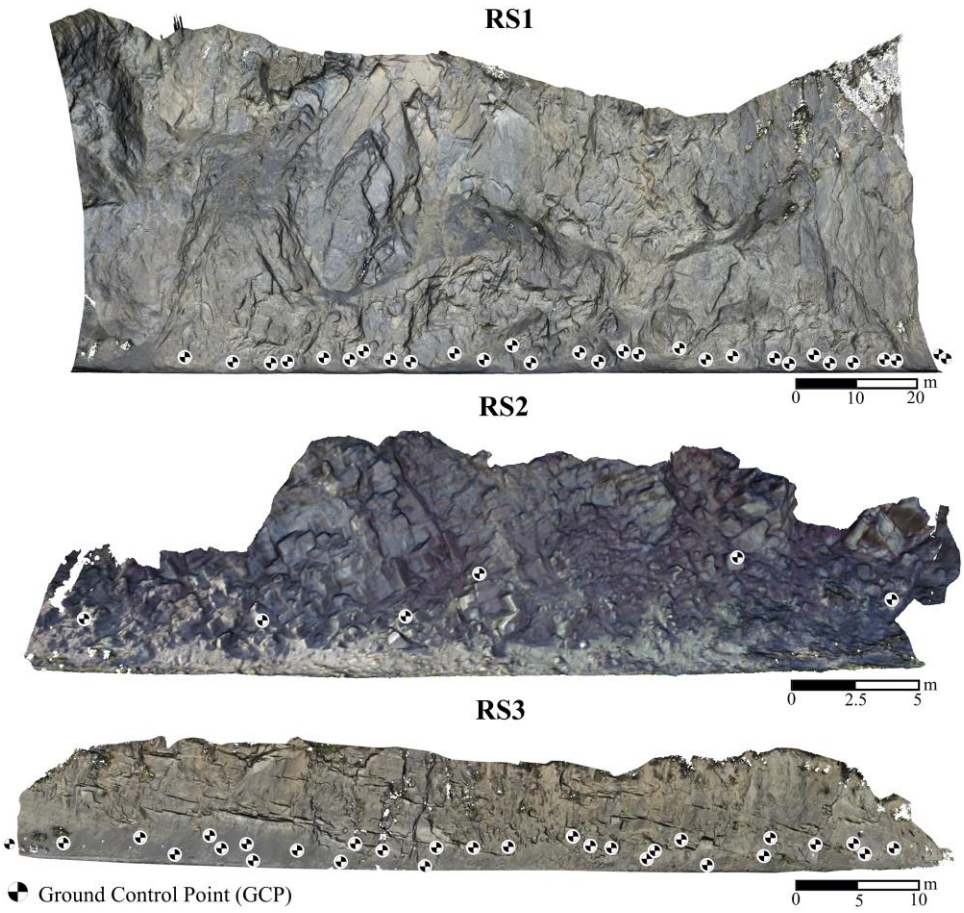

Fig. 2. SfM-derived 5 cm surface models of the three rock slopes (RS1, RS2, and RS3) with the layout of black & white targets used as ground control points (GCP).

Methodology

Data Collection

Survey Control. A survey control network was developed for each study site to ensure proper scaling of the SfM reconstructions and for geo-referencing of both the SfM and TLS data. The control network consisted of Static and Rapid Static (RS), Global Navigation Satellite System (GNSS) occupations, and paper-based black & white targets, which served as GCPs. Two types of paper-based GCPs were used, generic black & white targets, commonly used in TLS survey workflows, and PhotoScan branded targets which can be auto-extracted in the Agisoft PhotoScan

software (Agisoft, 2017). The layout of GCPs for each rock-slope site is presented in Fig. 2. Sites RS1 and RS3 have GCPs that are not located on the selected rock-slope surface. These GCPs were used during development of the SfM models; however, they do not lie within the clipped region of the rock-slope. Components of the survey control network were tied together using a Leica TS15 (1") total station instrument. Two total station positions were used to establish the control network for both RS1 and RS3. A single total station position was adequate for RS2 given its limited horizontal and vertical extent. Processing of the total station data and subsequent adjustment of the control network was performed in StarNet 8.0 (*Control Network Processing* Section). The control network was established in the Alaska State Plane Coordinate System Zone 4, North American Datum 1983 (2011) Epoch 2010.00. Orthometric heights were estimated in the North American Vertical Datum of 1988 by differencing the ellipsoid heights with geoid heights from GEOID 12A.

Two types of RS observations were collected: RS control points positioned along the highway and marked with a magnetic survey nail, and scan position occupations acquired using a scanner mounted GNSS receiver. A survey-grade GNSS receiver (Leica GS14) was set up over an established control point and served as a base station to post-process short (< 15 min) RS GNSS observations using relative positioning techniques.

RS control points were incorporated into the survey control network using a TS instrument, prism rod, and 360° prism. The center point of all black & white paper target placed within a scanned/imaged scene was acquired by the TS in reflectorless mode.

The TS was also used to acquire reflectorless points scattered across the rock-slope faces. The purpose of these points is twofold, first to serve as an independent reference for evaluating the accuracy of the TLS-derived surface models and second, to evaluate the accuracy of SfM models in portions of the rock-slope unoccupied by GCPs. The rock-slope TS points are not to be confused with the survey control network; they were simply acquired with the TS instrument during the development of the control network.

TLS Survey. TLS surveys were performed using a Riegl VZ-400 laser scanner following a stop-and-go scanning approach similar to that presented in (Olsen et al., 2009; Olsen et al., 2015) for efficient mobilization of equipment along the shoulder lane of the highway. The TLS configuration included a calibrated, digital SLR (Nikon D700) camera and survey-grade Leica GS14 GNSS receiver mounted on top with known calibrated offsets. Precise inclination sensors (±0.008°, 1-□) integrated into the TLS instrument (Silvia and Olsen, 2012) enable the scans to be

accurately leveled despite the unlevel wagon platform. Electronic Distance Measurement (EDM) scaling corrections were applied for atmospheric conditions, including temperature, pressure, and relative humidity. All scans had a field-of-view of 360° horizontally and +60° to -40° vertically relative to the horizontal plane. Scans were acquired from the shoulder opposite of the rock-slope at 40-60 m intervals (adapting to features of interest on the cliff) with an angular resolution of between 0.02 and 0.05°.

Prior to collection of TLS scans at each site, black and white pattern targets mounted to rigid clipboards were placed throughout the anticipated scanned scene.

UAS Imagery. Aerial photographs were obtained using a DJI Phantom 3 Professional quadcopter UAS platform. The Phantom 3 weighs 1.3 kg (including camera payload), is approximately 40-cm-wide, and has a flight endurance of about 20 minutes. The UAS platform includes an integrated 3-axis gimbal system to stabilize the camera during flight, thus minimizing vibration-induced blur in the aerial images. The gimbal provides a pitch range of -90° (i.e., nadir) to +30°, which can be adjusted in-flight using DJI's mobile flight control application GO. The Phantom 3's integrated camera has a 20 mm (35-mm equivalent) f/2.8 lens coupled with a 6.2 mm x 4.6 mm sensor that produces 12.4-megapixel images with an effective resolution of 4000 x 3000 pixels. Similar to the terrestrial images, the aerial photographs were obtained with a fixed focal length (i.e., no zooming), in bright daylight, and recorded in RAW image format. The UAS was flown in the manual mode (i.e., without a pre-programmed flight path) by a pilot positioned within sight of the aircraft at the base of each rock-slope. An automated flight plan solution that was capable of maintaining a safe distance from the rock-slopes while avoiding obstacles was not available. During the flight, a second crew member operated the UAS camera using the DJI GO application. The UAS was flown at altitudes ranging from approximately 10 m to 100 m above the base of each rock-slope. The aerial platform provided greater flexibility for positioning the camera system, allowing us to obtain images from a variety of perspectives including close-range views of incised and recessed morphological features (e.g. small gorges) and broad-range views of nearly the entire rock-slope. Attempts were made to capture imagery with the camera oriented approximately perpendicular to the rock-slope surface. In general, the aerial photographs of the rock-slope face were obtained in a gridlike pattern with ~8 m horizontal spacing along ~8 m-spaced lines of fixed altitude, resulting in approximately 80% overlap in the images. Photographs were captured at downward pitches (-60° to -10°), capturing benches and other features that were not visible from the ground. The median distance of the UAS from the rock-

slope was 11 m, 10 m, and 14 m for RS1, RS2, and RS3, respectfully. The UAS aerial photography required about 40 minutes to complete at each site, including time for at least one landing and re-launch sequence for battery replacement.

Terrestrial Imagery. Terrestrial photographs were acquired using a Sony Cyber-shot DSC-RX10 II digital camera with a 24-200 mm (35-mm equivalent) f/2.8 lens and 13.2 mm by 8.8 mm sensor, resulting in images with an effective resolution of 20.2 megapixels (5496 x 3672). Before the fieldwork in Alaska, we performed trial photography campaigns at a benchmarked outdoor test site to determine the optimal camera settings for the SfM acquisition. In our test trials, we obtained the most accurate results when the camera's focal length was fixed at 24 mm, and the aperture was set to f/5.6. Adopting these settings, we photographed the rock-slopes in bright ambient daylight (flash was disabled) and recorded the images in RAW format. Although storage intensive, the RAW image format produces minimally processed "digital negatives" whose white balance and color grading can be subsequently adjusted, if necessary. The photographer shot the images in handheld mode from a position on the far road shoulder of the 2-lane highway located at the base of the rock-slopes. The camera-to-subject distances varied depending on the width of the shoulder area. Median camera-to-subject distances were 20 m, 9 m, and 10 m for RS1, RS2, and RS3, respectfully. Photograph locations were obtained at ~5 m intervals along the base of the rock-slopes, with the aim of having at least 50% vertical and horizontal overlap in the neighboring images. In general, single photographs from multiple perspectives were preferred over multiple photographs taken by pivoting from a single location. The terrestrial photography required about an hour to complete at each site.

Data Processing

Control network processing. The GNSS base station coordinates were established using the Static processing available through the National Geodetic Survey's Online Positioning User Service (OPUS-S). RS GNSS control points were processed against the base station using baseline vector processing in Leica Geo Office v.8.3 (Leica Geosystems, 2012). These coordinates were also obtained using rapid-static processing available through the National Geodetic Survey's Online Positioning User Service (OPUS-RS) for validation.

For each site, a 3D, constrained, least squares adjustment of the control network was completed using StarNet 8.0 to produce the final coordinates and uncertainties for the control targets and reflectorless measurements on the

rock-slope surfaces. The following observations were input for the adjustment: GNSS control point coordinates and associated uncertainties obtained from OPUS (peak-to-peak error) and OPUS-RS (standard deviations), GNSS baseline vectors between the base station and rover positions with associated covariance matrices, and the measured distances, horizontal angles, vertical angles, and uncertainties for the total station measurements for each setup. The GNSS baseline vector uncertainties were scaled by a factor of 25 to account for the overly optimistic estimates (sub-mm) obtained during baseline processing (Ovstedal, 2000; Kashani et al., 2004; Weaver et al., 2018). A Chi-square statistical test against the stochastic model was completed and passed at the 5% level. Estimated propagated errors of the coordinates for the stations were <1.5 cm (3D RMS) at the network level and <7mm (3D RMS) at the local level. Note that these estimates do not include geoid modeling error.

TLS Processing. Post-processing of TLS data is required to merge individual scans into a cohesive point cloud. This process requires adjustment of the position and orientation of a given scan location, resulting in a rigid-body transformation of the 3D point cloud acquired from that location. Information derived from the onboard inclination sensors, the top-mounted GNSS receiver and the relative position of GCP targets captured in the scan enable the determination of transformation parameters, including rotations and translations along orthogonal axes.

Prior to performing local registration of the point cloud data, individual scans were leveled in accordance with values reported by the onboard inclination sensors. Local registration and geo-referencing of the TLS data was performed in Leica Cyclone v.9.1 software (Leica Geosystems, 2015) using target matches and cloud-to-cloud surface matching constraints. The co-registered point clouds were subsequently geo-referenced using both the adjusted survey control network and the scan position coordinates derived from the top-mounted GNSS receiver.

Quality control of point cloud registrations included a review of misalignment error vectors for target constraints, a review of total error associated with cloud-to-cloud constraints, and visual inspection of registered point clouds, including cross-section inspection. Visual inspections of the registered point clouds were performed to identify the presence of any point cloud misalignment artifacts that would require re-registration.

SfM Processing. Image-based 3D reconstruction was performed using Agisoft PhotoScan Professional v.1.3.4 (Agisoft, 2017). Three models were developed for each study site: Ground (solely ground-based imagery), UAS (only the UAS imagery), and Combo (ground and UAS imagery). Prior to importing the digital images into

PhotoScan, the UAS-based images (DNG format) were processed using the DJI DNG Cleaner software and both the cleaned DNG and RAW images were converted to JPEG using the Adobe Lightroom software.

The "Align Photos" tool was used for initial camera alignment and subsequent development of a sparse 3D point cloud with the following settings: Accuracy = High, Generic preselection, Key point limit = 45,000, and Tie point limit = 4,000. Following the creation of the sparse point cloud, GCP coordinates derived from the survey control network for each site were imported. The "Detect Markers" tool was used to automatically extract the centers of any PhotoScan branded targets. The centers of additional non-PhotoScan targets were manually extracted from the imagery. All marker assignments, including those auto-extracted from PhotoScan targets, were reviewed to ensure proper extraction of GCP centers and to omit constraints relying on blurry images. After this thorough review, the "Optimize Cameras" tool recalculated external and internal orientation (including lens distortion parameters) of the camera(s) to refine all GCP markers. The "Build Dense Cloud" tool then generated the final high-resolution point cloud with the following settings: Quality = High, and Depth filtering = Mild.

Surface Generation. Finalized SfM and TLS point clouds were cropped to identical extents, including only portions of a given rock-slope to be studied. Coarse vegetation removal was performed by manually selecting and deleting regions of vegetation in the point cloud. Efforts were made to be consistent when performing manual vegetation removal; however, in many cases, vegetation in a given area appeared differently in the SfM and TLS datasets. For example, a dense shrub observed as a surficial shell of points in the SfM data may appear as a noisy fuzz of points in the TLS data resulting from the laser beam penetrating the foliage resulting in mixed pixels. 3D surface models (5 cm resolution) for each study site were created from the cropped and cleaned point cloud data using the optimal plane triangulation methodology presented in (Olsen et al., 2015).

Accuracy Assessment

Two independent references (both tied to the aforementioned control network) are available for assessing the accuracy of the SfM models: the TLS-derived surface models, and the rock-slope TS points. In this case, the TLS surface models are preferred over the rock-slope TS points because they offer many more nodes/vertices for 3D differencing. When comparing two surface models of similar extent, all nodes that comprise a surface mesh can be compared to those of the reference surface. The quantity of rock-slope TS points for the different study sites ranges

from 50 to 100 discrete points, which is far fewer than the 1 x 10^5 to 2 x 10^6 nodes made available by the surface models.

Prior to assessing the accuracy of the SfM-derived surface models, the accuracy of the TLS-derived models was evaluated using the rock-slope TS points. This important step validates the TLS surface models as an appropriate reference for assessing the accuracy of the SfM models. They also serve as an additional reference for assessing the accuracy of the SfM models.

Surface-to-surface (comparing TLS and SfM surfaces) and surface-to-point (comparing a surface to the rock-slope TS points) assessments were completed using the "Color from Distance" tool in Maptek I-Site Studio 6.0 software (Maptek, 2016). A maximum distance threshold of $\pm$ 0.20 m was chosen as not to include larger discrepancies associated with the presence of inconsistent vegetation removal. The reported distances represent 3D discrepancies measured along the surface normal of the base surface to the closest point or surface node. Comparison of the interpolated surface models was chosen instead of a solely point-to-point evaluation because the accuracy of surface models is more relevant to our preferred, unstable rock-slope assessment and monitoring techniques (Olsen et al., 2015; Dunham et al., 2017). In addition, point-to-point comparisons are more appropriate for preliminary error assessments as they are prone to outliers and differing point densities (Eltner et al., 2016). Nevertheless, point-to-point comparisons performed using CloudCompare software (Girardeau-Montaut, 2017) achieved similar results.

Quality Evaluation

The SfM quality evaluation focuses on the suitability of SfM for the assessment of rock-slopes. Multiple characteristics including point density, completeness, and the capabilities of SfM to capture surface morphology (e.g., slope and roughness) were evaluated relative to TLS.

Point density was determined by sub-sampling the TLS and SfM point clouds into 5 x 5 cm grid cells and recording the number of points within each cell. The completeness metric was determined based on relative values of model surface area at each site. A baseline surface area representing full completeness was established for each site based on the Combo SFM point cloud with surface data gaps (holes) filled. Small holes in the 3D surface models were filled using the thin plate spline technique presented in (Olsen et al., 2015). The Combo SfM model was assumed to be the most complete because of its use of both ground and UAS-based imagery which minimizes

the occurrence of data gaps. Completeness values were determined by comparing the surface area of a model with no hole filling to the site-specific baseline surface area representative of a complete model (Eq. 1).

$$Completeness = \left(\frac{Surf.\ Area\ of\ Model\ with\ out\ Holes\ Filled}{Surf.\ Area\ of\ Combo\ SfM\ Model\ with\ Holes\ Filled}\right) \times 100 \quad (1)$$

Comparative distribution plots were developed to present the differences in surface morphology captured by TLS and SfM methods. The chosen surface parameters include slope, surface roughness, and the Rockfall Activity Index (RAI). RAI is a point-cloud-derived, morphology-based classification methodology used to evaluate rockfall hazards (Dunham et al., 2017). Two types of surface roughness (standard deviation of slope) were examined: small window (SW) roughness, which is computed using a 35 x 35 cm window; and large window (LW) roughness utilizing an 85 x 85 cm window. The window sizes were selected because of their relevance to the RAI methodology.

Lastly, a visual qualitative inspection of the TLS and SfM derived point clouds was performed. Both TLS and SfM point clouds were added to the same 3D visualization for direct visual comparison allowing for detailed inspection of geometric discrepancies between the TLS and SfM datasets.

Results

SfM and TLS point cloud data attributes (Table 1) include the type of point cloud, the number of images used for SfM reconstruction or the number of scans for TLS data, the quantity of GCP targets used for registration, the total amount of points in the point cloud on the rock-slope surface, and the mean point density for each dataset.

Table I. Details of the SfM and TLS point clouds.

Site	*Approx. Slope Surface Area (m²)*	*Type*	*Number of Images/Scans*	*Number of GCPs*	*Total Points*	*Mean Point Density (pts/m²)*
RS1	9,300	Ground SfM	140	29	43,441,327	6,151
		UAS SfM	132	25	19,807,042	2,804
		Combo SfM	272	29	39,411,287	5,579
		TLS	6	29	55,681,383	7,875
RS2	450	Ground SfM	124	8	43,839,216	122,830
		UAS SfM	30	5	4,420,183	12,378
		Combo SfM	154	7	31,091,288	86,751
		TLS	3	10	12,095,566	33,871
RS3	1,680	Ground SfM	164	29	81,738,569	63,585
		UAS SfM	61	25	11,571,375	9,001
		Combo SfM	225	29	63,474,055	49,361
		TLS	5	30	27,881,655	21,684

The number of images and TLS scans, and GCPs used for RS1 and RS3 are very similar; however, their approximate surface areas are quite different (further discussed in Discussion section). Site RS2 required fewer images, TLS scans, and GCPs due to its relatively smaller horizontal extent. For RS1, the TLS point cloud has the largest number of points, followed by the Ground SfM, Combo SfM, and UAS SfM point clouds, listed in order of decreasing point count. The point count for RS2 and RS3 indicate a different trend in which the Ground SfM dataset has the largest quantity of points, followed by the Combo SfM, TLS, and UAS SfM datasets. A significant difference in total points exists between the TLS datasets for RS1 and RS2 despite the fact that there is a similar number of scans completed. This occurs predominately because the rock-slope is much taller for RS1. For all three rock-slope sites, the Ground SfM model has a greater number of points and higher mean point density when compared to the Combo SfM model. Average ground resolution (i.e., ground sampled distance (GSD)) of the SfM imagery as reported by PhotoScan is as follows: 7.12 mm/pixel, 12.5 mm/pixel, and 9.18 mm/pixel for the RS1 Ground, UAS, and Combo SfM models, respectfully; 1.77 mm/pixel, 5.85 mm/pixel, and 2.25 mm/pixel for the RS2 Ground, UAS, and Combo SfM models, respectfully; and 2.09 mm/pixel, 6.93 mm/pixel, and 2.94 mm/pixel for the RS3 Ground, UAS, and Combo SfM models, respectfully.

Accuracy Assessment

Rock-slope surface maps depicting the spatial distribution of geometric discrepancies identified between the SfM and TLS surface models were developed for each of the study sites (Fig. 3). The minimal discrepancy between the SfM and TLS surface models is represented by regions colored in green. Regions colored in shades of blue represent where the SfM surface is located in front of the TLS surface, and shades of red represent where the SfM surface is located behind the TLS surface model. Regions of the rock-slope colored magenta indicate surface discrepancies larger than a $\pm$ 0.2 m threshold to omit vegetation-derived discrepancies from the evaluation.

Similar error patterns are observed for the various SfM surface models depicted in Fig. 3. The Ground and Combo SfM surface models demonstrate close alignment with the TLS surfaces; while, the UAS SfM surfaces result in a distinct error pattern, which includes a discontinuity across the rock-slope face where discrepancies with the TLS surface transition from positive to negative. Statistics, including the mean, standard deviation, RMSE, and 95% confidence error of the 3D discrepancies of the surface-to-surface comparisons are included in Table 2. The percentage of the SfM-derived surface model in front of the TLS surface model is also provided. Values deviating significantly from 50% indicate a drifting trend for the SfM surface.

Results of the surface-to-surface comparison between SfM and TLS models indicate 3D errors at 95% confidence ranging from ±0.044 m to ±0.048 m for Ground SfM models, ±0.048 m to ±0.112 m for UAS SfM models, and from ±0.041 m to ±0.048 m for Combo SfM models. Likewise, the results of the surface-to-points comparison between TLS and SfM surface models and the rock-slope TS points are presented in Table 3. Comparison of the TLS surface models to the TS points indicates a consistent surface model accuracy of ±0.015 m at 95% confidence across all sites.

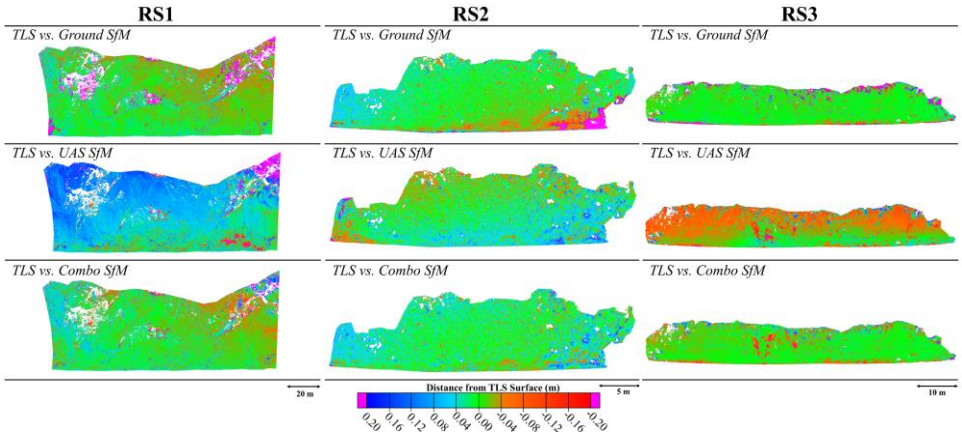

Fig. 3. Geometric discrepancies for RS3 identified by differencing TLS and SfM surface models.

Table II. Statistics regarding 3D discrepancies between SfM and TLS-derived 5 cm resolution 3D surfaces.

SfM Model	*Type*	*Mean Diff. (m)*	*σ (m)*	*RMSE (m)*	*Error 95% Conf. (m)*	*% of SfM in Front of TLS*
RS1	Ground SfM	-0.003	± 0.029	± 0.029	± 0.047	55.4
	UAS SfM	-0.051	± 0.046	± 0.069	± 0.112	94.1
	Combo SfM	-0.006	± 0.029	± 0.030	± 0.048	60.5
RS2	Ground SfM	-0.002	± 0.027	± 0.027	± 0.044	58.3
	UAS SfM	-0.010	± 0.028	± 0.030	± 0.048	65.3
	Combo SfM	-0.010	± 0.023	± 0.025	± 0.041	72.9
RS3	Ground SfM	0.000	± 0.030	± 0.030	± 0.048	56.9
	UAS SfM	0.020	± 0.036	± 0.041	± 0.066	23.0
	Combo SfM	0.003	± 0.026	± 0.027	± 0.043	43.8

Table III. Statistics regarding 3D geometric discrepancies between SfM and TLS-derived 5 cm resolution 3D surfaces and the Rock-Slope TS points.

Site	*Type*	*Mean Diff. (m)*	*σ (m)*	*RMSE (m)*	*Error 95% Conf. (m)*	*% of Surface in Front of TS Points*
RS1	Ground SfM	-0.001	± 0.015	± 0.015	± 0.025	57.14
	UAS SfM	-0.032	± 0.041	± 0.052	± 0.084	82.69
	Combo SfM	-0.006	± 0.020	± 0.021	± 0.033	56.19
	TLS	0.002	± 0.009	± 0.010	± 0.015	41.90
RS2	Ground SfM	0.002	± 0.024	± 0.025	± 0.040	48.98
	UAS SfM	0.006	± 0.029	± 0.029	± 0.047	36.73
	Combo SfM	-0.001	± 0.024	± 0.024	± 0.039	57.14
	TLS	0.003	± 0.009	± 0.009	± 0.015	31.25
RS3	Ground SfM	-0.001	± 0.008	± 0.008	± 0.013	63.86
	UAS SfM	0.013	± 0.025	± 0.028	± 0.046	22.89
	Combo SfM	-0.001	± 0.011	± 0.011	± 0.017	53.01
	TLS	0.001	± 0.009	± 0.009	± 0.014	55.42

Quality Evaluation

Point Density. Point density heat maps were developed for each of the three study sites (Fig. 4). The rock-slope point density maps demonstrate both the varying magnitude and spatial distribution of point density throughout the different SfM and TLS point cloud datasets. A smaller point density range was applied to the color ramp for RS2 to account for the lower point densities identified for RS2. The Ground SfM surface models for RS2 and RS3 are saturated with red due to their high point density relative to the other surface models generated for those sits. Comparative distribution plots of point density for the three rock-slope sites are presented in Fig. 5.

Similar trends in point densities are observed for sites RS2 and RS3. Study site RS1 demonstrates unique results with regards to the relative distributions of point density. For RS1, the TLS point cloud has the highest mean point density and standard deviation. The ranking of the remaining SfM datasets is Ground SfM, Combo SfM, and UAS SfM, listed in order of decreasing mean point density. The point density evaluation for RS2 and RS3 reveals a ranking for mean point density that differs from that observed for RS1. Listed in order of decreasing mean point density, the Ground SfM data has the highest mean, followed by the Combo SfM, TLS, and UAS SfM datasets. Additionally, a clear separation in point density is observed for RS2 and RS3; this separation is not as apparent for RS1. When comparing results for RS2 and RS3, the standard deviations for all datasets are higher for RS2, resulting in a larger range of point density values across the rock-slope. The mean point density of the RS1 SfM models is around an order of magnitude smaller than the SfM point densities reported for RS2 and RS3.

All point density distributions computed for the Ground SfM model have a noticeable increase in low point density values. This increase is attributed to the relatively large quantity of zero values added to the Ground SfM datasets to account for data gaps that contribute to the lower completeness percentage of these data. Zero values were added to all SfM and TLS datasets to account for data gaps; however, changes to the distributions were negligible given the high completeness percentage of all but the Ground SfM datasets.

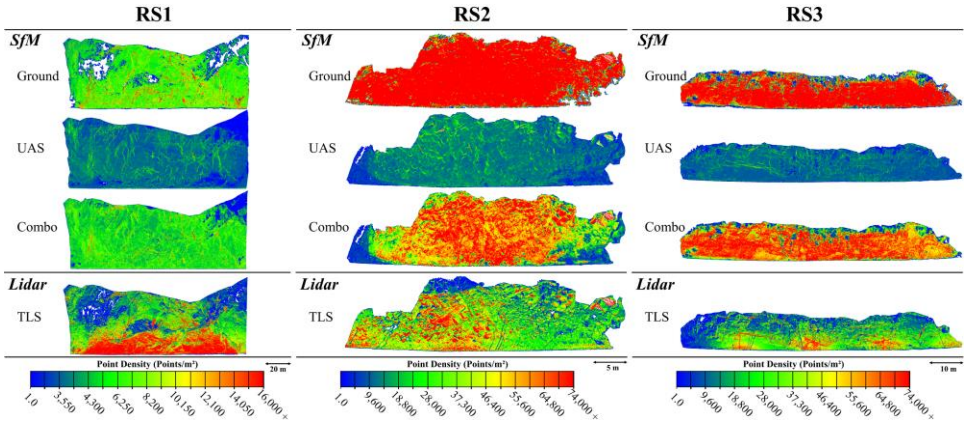

Fig. 4. Point density heat maps for RS3 SfM and TLS-derived 3D point cloud data.

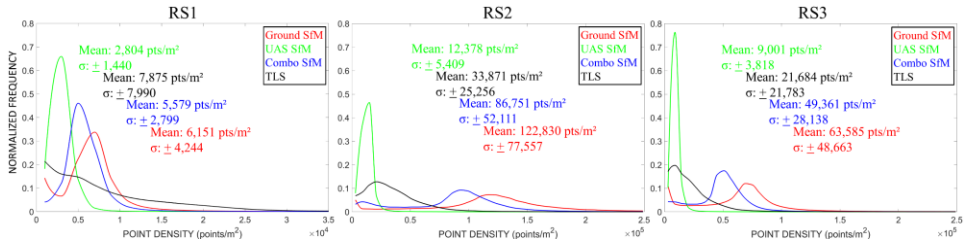

Fig. 5. Comparative distribution plots of point density for SfM and TLS datasets.

Completeness. Completeness of the surface models range from 89.4% to 99.5% for RS1, 96.9 % to 99.8% for RS2, and 94.4% to 99.5% for RS3. For all three study sites, the Ground SfM models result in the least complete surface model, and the UAS or the Combo SfM models are the most complete. Paradoxically, the Ground SfM models contained the largest number of points.

Surficial Parameters. Comparative distribution plots were developed to present the differences in surface morphology captured by TLS and SfM methods. Surface parameters evaluated for this study include slope, SW

surface roughness, and LW surface roughness (Figs. 6-8). All distribution plots were normalized to account for differences in completeness amongst the surface models.

Overall, the normalized distributions of slope for the surface models at each site are very similar. The results for RS1 indicate the distributions of slope for the Combo and UAS SfM models differ from the distributions of slope for the Ground SfM and TLS models. The Combo and UAS SfM datasets have a localized increase in slope values at around 40° that is not observed in the others.

With regard to mean of SW roughness, the UAS SfM model is most similar to the TLS data for RS1, and the Ground SfM model is most similar to the TLS data for Sites RS2 and RS3. When examining standard deviation of SW roughness, the Combo SfM model is most similar to the TLS data for Sites RS1 and RS3, and the Ground SfM model is most similar to TLS for RS2 (Fig. 7).

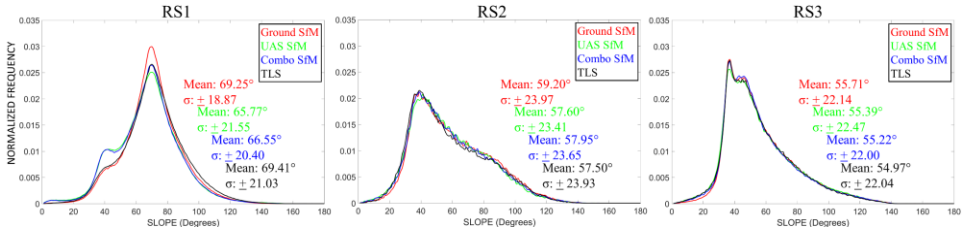

Fig. 6. Comparative distributions for surface slope.

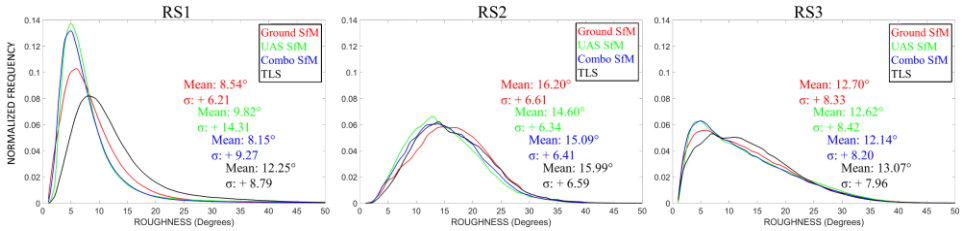

Fig. 7. Comparative distributions for small window (35x35 cm) roughness

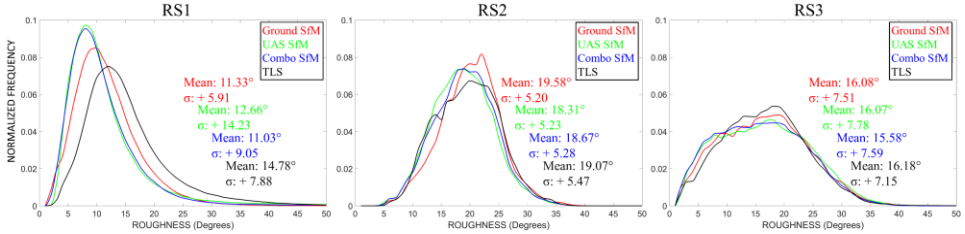

Fig. 8. Comparative distributions for large window (85x85 cm) roughness

For Site RS1, there is a clear separation in the distributions of SW roughness between the SfM and TLS datasets and the distributions for the Combo and UAS SfM models are very similar (Fig. 7). The TLS distribution of SW roughness for RS1 is significantly different from the SfM datasets, indicated by an average mean shift of + 3.4°. For Sites RS2 and RS3, the distributions of SW roughness for the Ground SfM data are slightly shifted toward a higher roughness when compared to the other SfM datasets. Results for RS2 indicate similar distributions of SW roughness for the Combo SfM and TLS datasets; however, the TLS and Ground SfM distributions become more aligned for SW roughness values > ~22°. The mean SW roughness values for the RS3 Combo SfM and TLS models are similar but, the distributions are different. The SW roughness distributions for the Combo SfM model has a clear increase in frequency at SW roughness values of ~5° that is not present in the TLS distribution (Fig. 7).

In general, the results of the LW surface roughness evaluation are similar to those reported for the SW surface roughness with a few subtle differences. In terms of the mean of LW roughness, the UAS SfM model is most similar to the TLS data for RS1, the Combo SfM model is most similar to the TLS data for RS2, and the Ground SfM is most similar for RS3. When examining standard deviation of LW roughness, the Combo SfM model is most similar to the TLS data for Sites RS1 and RS2, and the Ground SfM model is most similar to TLS for RS3 (Fig. 8).

For Sites RS2 and RS3, the distributions of LW roughness for the Ground and SfM data are slightly shifted toward a higher roughness when compared to the other SfM datasets. Results for RS2 indicate similar distributions of LW roughness for the Combo SfM and TLS datasets; however, the Combo SfM distribution has an increase in frequency at LW roughness values of ~15° with respect to the TLS distribution, and the Ground SfM model becomes more aligned with the TLS distribution for LW roughness values > ~25°. For Site RS3, the LW roughness distributions for all SfM models are shifted towards lower roughness values with respect to the TLS distributions. However, the SfM and TLS distributions become better aligned for LW roughness values > ~22°.

Rock-Slope Morphology Classification. The RAI classification evaluation is presented as comparative histogram plots in Fig. 9. A significant over-prediction of intact rock (I) occurs for RS1 followed by an under-prediction of the fragmented (Df), closely spaced (Dc), and widely to moderately spaced (Dw) discontinuous rock units, as well as steep (Os) and cantilever (Oc) overhangs when compared to the TLS surface. The distribution of RAI classifications for RS2 is similar amongst the SfM and TLS surface models. The most significant discrepancies are an over-prediction of Df and an under-prediction of Dw by the UAS SfM data. Similar to the results for RS1, we observe an

over-prediction of I and under-prediction of Dc for RS3; however, the discrepancies are not as large as those observed for RS1.

Overall, the RAI classifications for Ground SfM-derived surfaces are most similar to the RAI classifications determined for the TLS surfaces. Example RAI classification maps for RS1 are presented in Fig. 10. The over-prediction of RAI Class I observed in Fig. 9 is depicted in Fig. 10 by the dominance of bright green observed for the SfM surface model. The insets presented in Fig. 10 provide a close-up view of the RAI classifications for each of the surface models. The TLS inset shows the prevalence of Dc and Dw classifications that is not observed in the insets of the SfM-derived surface.

Visual inspection. Qualitative inspection of the TLS and SfM point cloud data revealed a prevalence of over-smoothing in the UAS and Combo SfM data. Many of the sharp edges associated with rock outcrop discontinuities, were observed to be more round and smooth when compared side-by-side with the TLS point cloud data. Over-smoothing was not as apparent in the Ground SfM point cloud data. Simultaneous visualization of the TLS and SfM point clouds also revealed the ability of UAS-based SfM to, in some scenarios, outperform TLS with respect to seeing beneath vegetation. This is attributed to the ability of UAS to occupy numerous advantageous points of view, allowing imaging around and beneath spurious vegetation (e.g., small trees and isolated shrubs). In areas of dense ground cover, TLS is observed to outperform UAS-based SfM methods.

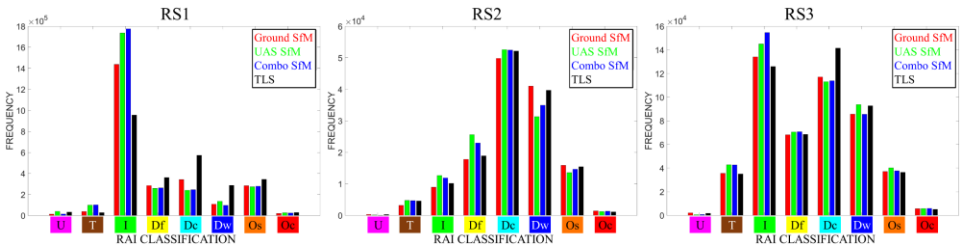

Fig. 9. Comparative histogram plots for RAI classification. RAI classifications are as follows: Unclassified (U), Talus (T), Intact Rock (I), Fragmented discontinuous rock (Df), Closely spaced discontinuous rock (Dc), Widely to moderately spaced discontinuous rock (Dw), Steep overhang (Os), and Cantilever overhang (Oc).

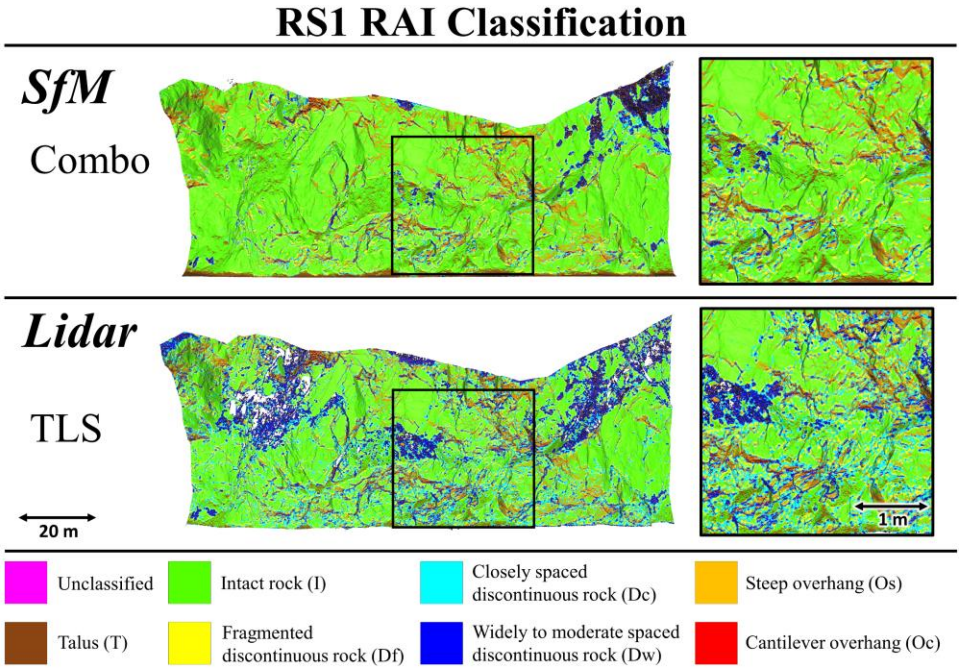

Fig. 10. RAI classification for RS1.

Discussion

For study sites RS2 and RS3, the total number of points for the Ground SfM datasets is about three times that of the TLS point clouds. This is not the case for RS1 where the discrepancy may be attributed to differences in image acquisition that stem from both technique and the relatively large vertical and horizontal extent of RS1. Twenty-four additional images were used to create the Ground SfM point cloud for RS3 when compared to RS1. In retrospect, this amount is inadequate given RS1 is ~30 m longer and ~ 50 m higher than RS3. Nevertheless, when attempting to capture a large rock-slope like RS1 with overlapping handheld imagery, it can be difficult to judge if enough images have been acquired with sufficient overlap.

The significant difference in TLS total points between sites RS1 and RS3 is attributed to differences is scanning geometry. Given the larger vertical extent and near vertical orientation of RS1, the TLS instrument was placed further away from the slope than for RS3 to ensure capture of the upper reaches. Increasing the distance between the TLS instrument and the area of interest will increase point spacing and decrease the total quantity of points, assuming the scanning resolution is unchanged.

Having a greater number of points and higher mean point density for the Ground SfM models when compared to the Combo SfM models is counterintuitive given the additional images used to generate the Combo models.

When including more images in an SfM reconstruction, one would expect the point quantity to increase. It is possible that this peculiar behavior stems from some automated optimization routine in PhotoScan that omits images and associated points if other imagery is available for a given region and is thought to be of higher quality. Further investigation is required to validate this possibility.

It is worth noting that the Combo SfM models generated for this study used an average of 217 images per site, compared to an average of 5 TLS scans per site. Assuming a reasonable scanning resolution is chosen, acquisition of 5 TLS scans can be performed in approximately the same amount of time as acquiring a total of 217 images gathered with both UAS and ground-based cameras. In addition, the efficiency of TLS acquisition could be further increased by following direct geo-referencing techniques that eliminate the need for placing GCPs (Olsen et al., 2009; Silvia and Olsen, 2012; Olsen et al., 2015), a technique currently being researched and evaluated (Carbonneau and Dietrich, 2017) but not yet widely available for SfM image acquisition campaigns that need to meet accuracies similar to those achievable with TLS. Mobile laser scanning (MLS) is a possible alternative for surveying these road cuts; however, the point density of MLS data is often significantly lower than that for static TLS data. With regard to road cuts, car/truck-based MLS can suffer from more severe point of view limitations than TLS. Because an MLS system commonly drives along the road, the resulting view of the rock-slope is more restricted when compared to the field of view of a TLS system set up across the road in the opposing road shoulder. In a scenario where the geospatial extent of a study area is significantly larger than that of this study, the efficiency benefits of UAS-based SfM are clear. TLS acquisition over large geospatial extents becomes time-consuming due to the mobilization of equipment from one scanning position to another. A UAS can cover these larger areas relatively quickly and efficiently and is not limited by hard to navigate terrain.

Accuracy Assessment

There is good agreement between both the Ground and Combo SfM surface models and the TLS-derived surfaces. Results indicate accuracies (95% confidence) ranging between $\pm$ 0.044 m and $\pm$ 0.048 m for Ground SfM, $\pm$ 0.041 m and $\pm$ 0.048 m for Combo SfM, and $\pm$ 0.0748 m and $\pm$ 0.112 m for UAS SfM model. Discrepancies between the UAS SfM models and the TLS surfaces follow a pattern in which the intersection of the two planes follow a path roughly parallel to the layout of the GCPs placed along the base of the slope. For RS1, the UAS SfM model is tilted such that 94.1% of the surface lies in front of the TLS surface. This same behavior is observed across

the three study sites; however, the percentage of SfM surface that lies in front of the TLS surface changes. The percentages are more balanced in the case of RS2, with 65.3% in front of the TLS surface. The presence of a clear intersection between the UAS SfM and TLS surfaces that appear to be associated with the layout of the GCPs indicates the lack of localized regions of significant deformation in the SfM surface that would affect the relative accuracy of the model. This differencing pattern is indicative of a global geo-referencing error as opposed to localized geometric distortions. The increased error identified in the UAS SfM models is attributed to both the inability to extract all GCPs in the UAS-based imagery, as well as, difficulties in accurately extracting the center of GCPs in the UAS imagery. Accurate extraction of GCPs is made difficult by the presence of pixilation in the imagery resulting from sampling at a large GSD relative to the ground-based imagery.

Ground-based SfM can result in high accuracy 3D data; however, it is plagued by numerous occlusions, similar to and often more severe than those seen in TLS data. The TLS outperformed ground-based SfM with respect to completeness even though images were acquired from many more locations/points of view than TLS scan positions (Table 1). This effect is likely attributed to the fundamental difference in passive and active remote sensing techniques employed by digital photography and TLS, respectively. In this case, the use of an active light source allowed TLS to capture meaningful geometric data at further distances than the handheld camera used for SfM image acquisition. While the TLS models were able to obtain more sampling directly below thick vegetation for creating a bare-earth surface model, the UAS SfM models demonstrated superior performance in capturing bare-earth behind and around sparser vegetation due to the flexible look angle.

Results of the surface-to-surface and surface-to-points (TS points) accuracy assessments reveal a consistent accuracy ranking of the SfM surface models, except for RS3. For RS1 and RS2, the Ground SfM model was identified as the most accurate based on the mean difference between the surface models and the references, followed by the Combo, and UAS SfM models. The accuracy assessments for RS3 indicate different accuracy rankings; however, this is reasonable given the similarity in accuracy reported for the Ground and Combo SfM models. Results of the rock-slope TS point accuracy assessment indicate higher accuracies when compared to the surface-to-surface assessment, which is a result of the significantly smaller sample size of differencing measurements used. The TS points accuracy evaluation validated the systematic accuracy of the TLS data, confirming TLS data is an appropriate choice for assessing the accuracy of SfM data. Additionally, The TS point accuracy assessment revealed relatively balanced proportions of TLS data located behind and in front of the TS

points, whereas, the SfM models were found to have variable proportions lying behind and in front of the TS reference points.

The Combo SfM models, which include both UAS and ground-based imagery, provide accuracies comparable to ground-based SfM while maintaining the completeness achieved with UAS image acquisition. Using both UAS and ground-based imagery for a SfM reconstruction exploits both the improved access afforded by a UAS and the resolution achieved from a ground-based handheld camera.

Quality Evaluation

Point Density. All SfM point clouds were found to have a more uniform point density when compared to TLS datasets, which is beneficial (visually, computationally, and accuracy-wise) in developing surface models with more consistent mesh elements and more uniform vertices for interpolation. Point density hotspots (Fig. 4) are a common occurrence in TLS point cloud data because scanning occurs at fixed angular increments, resulting in increased point spacing with distance for a given angular increment. Portions of the scanned environment that are close to a given scan position will have a significantly higher point density. Additionally, surfaces that are orthogonal to the laser pulse direction have a higher point density relative to surfaces that are oblique.

Completeness. The Combo and UAS SfM surface models are the most complete and Ground SfM models are the least complete, despite the fact that the Ground SfM models also have the greatest number of total points. This result is attributed to the resolution and GSD of the handheld imagery used to generate the Ground SfM reconstructions. Even though the Combo SfM models utilized more imagery and are more complete, they include fewer points due to the incorporation of lower resolution UAS-based imagery with a larger GSD.

Surficial Parameters. The localized increase in surface slope values of ~40° observed for RS1 (Fig. 6) represents regions of the rock-slope captured well with UAS and poorly captured with TLS and ground-based SfM. The majority of RS1 has a slope of ~60 to 80°; however, localized benches within the rock-slope are laid back at a shallower slope of between 40 and 45°. These localized benches proved difficult to capture with ground-based methods but were captured well with the advantageous point of view afforded by the UAS. Given the smaller

vertical extent of RS2 and RS3, the majority of the slope was visible to both aerial and terrestrial capture methods. As such, we observe very similar distributions of surface slope among the SfM and TLS datasets.

The evaluation of SW and LW roughness reveals evidence for the over-smoothing of the UAS and Combo SfM data observed during the qualitative visual inspection. Across all three study sites, we observe a bias of UAS and Combo SfM data towards lower roughness values when compared to TLS, which is likely a result of the lower resolution, higher GSD images contributed by the UAS. The distributions for SW and LW roughness for the Ground SfM datasets correlate well with the TLS distributions; however, as previously discussed, the Ground SfM models are deficient with respect to completeness. In general, the roughness distributions for the SfM surface models are found to align best with the TLS distribution in the right (upper) half of the distribution. This suggests that SfM is better suited for capturing surfaces with higher roughness as opposed to smoother surfaces.

Rock-Slope Morphology Classification. The discrepancies in RAI classification observed for RS1 are attributed to the large vertical extent of the rock-slope combined with the UAS imagery acquisition strategy. Results of the accuracy and roughness evaluations for RS1, support the unconservative RAI classification discrepancies observed for RS1. The use of a consumer-grade UAS (DJI Phantom 3 Professional) combined with flight limitations associated with the active roadway resulted in the acquisition of imagery of insufficient resolution and GSD. RAI classification of RS1 could be improved by using a higher resolution camera and/or gaining approval to fly closer to the rock-slope. Fewer discrepancies in RAI classification were observed for RS2 and RS3 because of their relatively smaller vertical extents. For RS2 and RS3, the ground-based imagery acquired with a handheld camera captured a majority of the slope, providing the detail necessary to assist the UAS imagery during SfM reconstruction.

Conclusion

Based on results of the accuracy assessment, SfM photogrammetry used in this study is not as accurate as TLS, but is an appropriate tool for rock-slope assessment, assuming the images are tied to a rigorous survey control network by way of GCPs. Use of a survey control network enables accurate scaling and geo-referencing of the resulting 3D point cloud data. While, the equipment needed to perform SfM (e.g., digital camera, UAS) is around two orders of magnitude less expensive than TLS, it is important to consider the significant cost of survey

equipment needed to establish appropriate control. Also, the additional time required to setup the control network is often neglected when SfM acquisition times are discussed.

It is also imperative that an appropriate quantity of images be acquired with adequate overlap – a difficult task to judge in the field when utilizing manual image acquisition methods, as was done in this study. UAS imagery was not acquired using an automated flight plan due to the lack of a flight planning solution that is compatible with vertical features (e.g., a rock-slope) and can be trusted in an obstacle rich environment.

It is undeniable that UAS-based SfM techniques offer superior color imagery and accessibility when compared to traditional TLS techniques. While a key benefit of TLS is its ability to penetrate through gaps in vegetation while the SfM cannot directly penetrate, the flexibility in positioning the UAS from different vantage points can result in improved ground coverage in some vegetation cover.

The Combo SfM models were found to benefit from the improved completeness and accuracy of the UAS and Ground SfM models, respectively. Ground-based imagery also served to capture imagery under rock outcrop overhangs where the UAS used for this study was unable to view. The inability of the UAS to see under overhangs is attributed to the placement of the camera under the body of the aircraft – this effect could be mitigated by using a UAS with a front mounted camera that can rotate to achieve an unobstructed view above the horizontal plane. It may also be possible to omit acquisition of ground-based imagery if a digital image sensor of increased size and resolution is used on the UAS and/or the UAS can fly closer to the rock-slope. For example, the handheld camera used for this study has an image sensor which is approximately twice the size and resolution of the sensor used in the UAS camera. If the handheld camera was mounted on the UAS, and the UAS was able to maintain a GSD similar to that achieved by ground-based image acquisition, the UAS-based imagery likely would result in a SfM reconstruction of similar accuracy and quality to that of the Ground SfM models.

With regard to monitoring rock-slopes using SfM techniques, caution must be exercised when performing change detection with SfM-derived point clouds and surface models. Artifacts, such as over-smoothing and geometric inconsistencies stemming from differences in image acquisition (e.g., lighting conditions and overlap) have potential to introduce error into detection of small changes. The inherent variability in SfM-derived geometry is demonstrated by the results of the TS point accuracy assessment. For the SfM-derived surface models, the accuracy and proportions of positive and negative discrepancies were found to be quite variable when compared to the consistent TLS results (Table 3). Useful studies have evaluated the performance of SfM with regards to change

detection (Lato et al., 2015b; James et al., 2017b); however, further work is needed to improve the threshold of change that can consistently be detected on rock-slopes with SfM techniques.

The accuracies presented in this paper serve as an example of what can be achieved with SfM techniques when following sound surveying methods. Given the variety of environments where these techniques can be employed, as well as, the plethora of available tools/instruments, it is likely that better or worse results could be achieved. The situation is further complicated by the difference in factors that contribute to uncertainty for TLS and SfM techniques. For TLS and total stations, factors such as range, incidence angle, and internal calibration play a major role in the propagation of uncertainty. For SfM, uncertainty is introduced through errors in the determination of exterior and interior orientation of the exposure stations, lens distortion, lighting conditions, and uncertainty in the automated process of keypoint matching, to name a few. Devising a real-world experiment that accounts for all the possible interactions amongst these factors is improbable. Evaluation of SfM experiments performed with simulated imagery of virtual, computer-generated environments provides an opportunity to further our understanding of how these factors may influence SfM point cloud quality and accuracy (Slocum and Parrish, 2017).

Acknowledgements

Funding for this research was provided by the Pacific Northwest Transportation Consortium (PacTrans) and Alaska Department of Transportation and Public Facilities. Leica Geosystems, David Evans and Associates, and Maptek provided software and hardware used in this study. Jeff Hollingsworth (University of Alaska, Anchorage) provided equipment and assistance in this study. Alireza Kashani assisted with the field work.

REFERENCES

Abellán, A., Calvet, J., Vilaplana, J.M., and Blanchard, J., 2010. Detection and spatial prediction of rockfalls by means of terrestrial laser scanner monitoring. Geomorphology, 119(3–4): 162–171.

Abellán, A., Jaboyedoff, M., Oppikofer, T., and Vilaplana, J.M., 2009. Detection of millimetric deformation using a terrestrial laser scanner: experiment and application to a rockfall event. Natural Hazards and Earth System Sciences, 9(2): 365–372.

Abellán, A., Oppikofer, T., Jaboyedoff, M., Rosser, N.J., Lim, M., and Lato, M.J., 2014. Terrestrial laser scanning of rock slope instabilities. Earth Surface Processes and Landforms, 39(1): 80–97.

Agisoft., 2017. PhotoScan.

Alba, M., Roncoroni, F., and Scaioni, M., 2009. Application of TLS for change detection in rock faces. 99–104.

Alba, M. and Scaioni, M., 2010. Automatic detection of change and deformation in rock faces by terrestrial laser scanning. Commission V Mid-Term Symposium on Close Range Image Measurement Techniques, 11–16.

Al-Rawabdeh, A., He, F., Moussa, A., El-Sheimy, N., and Habib, A., 2016. Using an Unmanned Aerial Vehicle-Based Digital Imaging System to Derive a 3D Point Cloud for Landslide Scarp Recognition. Remote Sensing, 8(2): 95.

Belowich, M., 2006. Matanuska Coal Field. Field Guide, Anchorage Alaska. Alaska Geological Society.

Bemis, S.P., Micklethwaite, S., Turner, D., et al., 2014. Ground-based and UAV-Based photogrammetry: A multi-scale, high-resolution mapping tool for structural geology and paleoseismology. Journal of Structural Geology, 69, Part A163–178.

Budetta, P. and Nappi, M., 2013. Comparison between qualitative rockfall risk rating systems for a road affected by high traffic intensity. Natural Hazards and Earth System Sciences, 13(6): 1643–1653.

Carbonneau, P.E. and Dietrich, J.T., 2017. Cost-effective non-metric photogrammetry from consumer-grade sUAS: implications for direct georeferencing of structure from motion photogrammetry. Earth Surface Processes and Landforms, 42(3): 473–486.

Chandler, J.H. and Buckley, S., 2016. Structure from motion (SFM) photogrammetry vs terrestrial laser scanning. In: M.B. Carpenter and C.M. Keane, eds., Geoscience Handbook 2016: AGI Data Sheets. American Geosciences Institute.

Dunham, L., Wartman, J., Olsen, M.J., O'Banion, M., and Cunningham, K., 2017. Rockfall Activity Index (RAI): A lidar-derived, morphology-based method for hazard assessment. Engineering Geology, 221184–192.

Eltner, A., Kaiser, A., Castillo, C., Rock, G., Neugirg, F., and Abellán, A., 2016. Image-based surface reconstruction in geomorphometry - merits, limits and developments. Earth Surface Dynamics, 4(2): 359–389.

Fassi, F., Fregonese, L., Ackermann, S., and Troia, V.D., 2013. Comparison Between Laser Scanning and Automated 3D Modelling Techniques to Reconstruct Complex and Extensive Cultural Heritage Areas. ISPRS - International Archives of the Photogrammetry, Remote Sensing and Spatial Information Sciences, XL-5-W173–80.

Fernández, T., Pérez, J.L., Cardenal, F.J., et al., 2015. Use of a Light UAV and Photogrammetric Techniques to Study the Evolution of a Landslide in Jaen (Southern Spain). ISPRS - International Archives of the Photogrammetry, Remote Sensing and Spatial Information Sciences, Copernicus GmbH, 241–248.

Fernández, T., Pérez, J.L., Cardenal, J., Gómez, J.M., Colomo, C., and Delgado, J., 2016. Analysis of Landslide Evolution Affecting Olive Groves Using UAV and Photogrammetric Techniques. Remote Sensing, 8(10): 837.

Fonstad, M.A., Dietrich, J.T., Courville, B.C., Jensen, J.L., and Carbonneau, P.E., 2013. Topographic structure from motion: a new development in photogrammetric measurement. Earth Surface Processes and Landforms, 38(4): 421–430.

Gigli, G. and Casagli, N., 2011. Semi-automatic extraction of rock mass structural data from high resolution LIDAR point clouds. International Journal of Rock Mechanics and Mining Sciences, 48(2): 187–198.

Girardeau-Montaut, D., 2017. Cloud Compare Open Source Software.

Greenwood, W., Zekkos, D., Lynch, J., Bateman, J., Clark, M.K., and Chamlagain, D., 2016. UAV-Based 3-D Characterization of Rock Masses and Rock Slides in Nepal. American Rock Mechanics Association.

Harwin, S. and Lucieer, A., 2012. Assessing the Accuracy of Georeferenced Point Clouds Produced via Multi-View Stereopsis from Unmanned Aerial Vehicle (UAV) Imagery. Remote Sensing, 4(6): 1573–1599.

Hungr, O., Leroueil, S., and Picarelli, L., 2014. The Varnes classification of landslide types, an update. Landslides, 11(2): 167–194.

Jaboyedoff, M., Oppikofer, T., Abellán, A., et al., 2012. Use of LIDAR in landslide investigations: a review. Natural Hazards, 61(1): 5–28.

James, M.R. and Robson, S., 2012. Straightforward reconstruction of 3D surfaces and topography with a camera: Accuracy and geoscience application. Journal of Geophysical Research: Earth Surface, 117(F3): F03017.

James, M.R., Robson, S., d'Oleire-Oltmanns, S., and Niethammer, U., 2017a. Optimising UAV topographic surveys processed with structure-from-motion: Ground control quality, quantity and bundle adjustment. Geomorphology, 280(Supplement C): 51–66.

James, M.R., Robson, S., and Smith, M.W., 2017b. 3-D uncertainty-based topographic change detection with structure-from-motion photogrammetry: precision maps for ground control and directly georeferenced surveys. Earth Surface Processes and Landforms, 42(12): 1769–1788.

Javadnejad, F. and Gillins, D.T., 2016. Unmanned Aircraft Systems-Based Photogrammetry for Ground Movement Monitoring. American Society of Civil Engineers, 1000–1011.

Kashani, I., Wielgosz, P., and Grejner-Brzezinska, D.A., 2004. On the reliability of the VCV Matrix: A case study based on GAMIT and Bernese GPS Software. GPS Solutions, 8(4): 193–199.

Kemeny, J. and Turner, K., 2008. Ground-based LiDAR Rock Slope Mapping and Assessment. Federal Highway Administration.

Kromer, R.A., Abellán, A., Hutchinson, D.J., Lato, M., Edwards, T., and Jaboyedoff, M., 2015. A 4D Filtering and Calibration Technique for Small-Scale Point Cloud Change Detection with a Terrestrial Laser Scanner. Remote Sensing, 7(10): 13029–13052.

Lato, M., Hutchinson, J., Diederichs, M., Ball, D., and Harrap, R., 2009. Engineering monitoring of rockfall hazards along transportation corridors: using mobile terrestrial LiDAR. Natural Hazards and Earth System Sciences, 9(3): 935–946.

Lato, M.J., Gauthier, D., and Hutchinson, D.J., 2015a. Rock Slopes Asset Management: Selecting the Optimal Three-Dimensional Remote Sensing Technology. Transportation Research Record: Journal of the Transportation Research Board, 25107–14.

Lato, M.J., Hutchinson, D.J., Gauthier, D., Edwards, T., and Ondercin, M., 2015b. Comparison of airborne laser scanning, terrestrial laser scanning, and terrestrial photogrammetry for mapping differential slope change in mountainous terrain. Canadian Geotechnical Journal, 52(2): 129–140.

Leica Geosystems., 2012. Leica Geo Office Software.

Leica Geosystems., 2015. Cyclone Software. Leica Geosystems.

Lim, M., Petley, D.N., Rosser, N.J., Allison, R.J., Long, A.J., and Pybus, D., 2005. Combined Digital Photogrammetry and Time-of-Flight Laser Scanning for Monitoring Cliff Evolution. The Photogrammetric Record, 20(110): 109–129.

Lim, M., Rosser, N.J., Allison, R.J., and Petley, D.N., 2010. Erosional processes in the hard rock coastal cliffs at Staithes, North Yorkshire. Geomorphology, 114(1–2): 12–21.

Lucieer, A., Jong, S.M. de, and Turner, D., 2014. Mapping landslide displacements using Structure from Motion (SfM) and image correlation of multi-temporal UAV photography. Progress in Physical Geography, 38(1): 97–116.

Manousakis, J., Zekkos, D., Saroglou, F., and Clark, M., 2016. Comparison of UAV-Enabled Photogrammetry-Based 3D Point clouds and Interpolated DSMs of Sloping Terrain for Rockfall Hazard Analysis. ISPRS - International Archives of the Photogrammetry, Remote Sensing and Spatial Information Sciences, Copernicus GmbH, 71–77.

Maptek., 2016. I-Site Studio Software.

Murphy, R.R., Duncan, B.A., Collins, T., et al., 2016. Use of a Small Unmanned Aerial System for the SR-530 Mudslide Incident near Oso, Washington. Journal of Field Robotics, 33(4): 476–488.

Niethammer, U., James, M.R., Rothmund, S., Travelletti, J., and Joswig, M., 2012. UAV-based remote sensing of the Super-Sauze landslide: Evaluation and results. Engineering Geology, 1282–11.

Olsen, M., Wartman, J., McAlister, M., et al., 2015. To Fill or Not to Fill: Sensitivity Analysis of the Influence of Resolution and Hole Filling on Point Cloud Surface Modeling and Individual Rockfall Event Detection. Remote Sensing, 7(9): 12103–12134.

Olsen, M.J., 2013. In Situ Change Analysis and Monitoring through Terrestrial Laser Scanning. Journal of Computing in Civil Engineering, 29(2).

Olsen, M.J., Johnstone, E., Driscoll, N., Ashford, S.A., and Kuester, F., 2009. Terrestrial Laser Scanning of Extended Cliff Sections in Dynamic Environments: Parameter Analysis. Journal of Surveying Engineering, 135(4): 161–169.

Ovstedal, O., 2000. Single Processed Independent and Trivial Vectors in Network Analysis. Journal of Surveying Engineering, 126(1): 18–25.

Pantelidis, L., 2009. Rock slope stability assessment through rock mass classification systems. International Journal of Rock Mechanics and Mining Sciences, 46(2): 315–325.

Pierson, L., 2013. Chapter 3: Rockfall Hazard Rating System. In: K. Turner and R.L. Schuster, eds., Rockfall Characterization and Control. Transportation Research Board.

Rabatel, A., Deline, P., Jaillet, S., and Ravanel, L., 2008. Rock falls in high-alpine rock walls quantified by terrestrial lidar measurements: A case study in the Mont Blanc area. Geophysical Research Letters, 35(10): .

Rosser, N., Lim, M., Petley, D., Dunning, S., and Allison, R., 2007. Patterns of precursory rockfall prior to slope failure. Journal of Geophysical Research: Earth Surface, 112(F4): .

Rosser, N.J., Petley, D.N., Lim, M., Dunning, S.A., and Allison, R.J., 2005. Terrestrial laser scanning for monitoring the process of hard rock coastal cliff erosion. Quarterly Journal of Engineering Geology and Hydrogeology, 38(4): 363–375.

Silvia, E.P. and Olsen, M.J., 2012. To Level or Not to Level: Laser Scanner Inclination Sensor Stability and Application. Journal of Surveying Engineering, 138(3): .

Slocum, R.K. and Parrish, C.E., 2017. Simulated Imagery Rendering Workflow for UAS-Based Photogrammetric 3D Reconstruction Accuracy Assessments. Remote Sensing, 9(4): 396.

Trop, J.M., Cole, R.B., Sunderlin, D., Hults, C., and Todd, E., 2015. Bedrock geology of the Glenn Highway from Anchorage to Sheep Mountain, Alaska. http://archives.datapages.com/data/alaska/data/040/1_akgs0400001.htm.

Turner, D., Lucieer, A., and de Jong, S.M., 2015. Time Series Analysis of Landslide Dynamics Using an Unmanned Aerial Vehicle (UAV). Remote Sensing, 7(2): 1736–1757.

Turner, K. and Jayaprakash, G.P., 2013. Introduction. In: K. Turner and R.L. Schuster, eds., Rockfall Characterization and Control. Transportation Research Board.

Weaver, B., Gillins, D.T., and Dennis, M., 2018. Hybrid Survey Networks: Combining Real-Time and Static GNSS Observations for Optimizing Height Modernization. Journal of Surveying Engineering, 144(1): 05017006.

Westoby, M.J., Brasington, J., Glasser, N.F., Hambrey, M.J., and Reynolds, J.M., 2012. "Structure-from-Motion" photogrammetry: A low-cost, effective tool for geoscience applications. Geomorphology, 179(Supplement C): 300–314.

Wilkinson, M.W., Jones, R.R., Woods, C.E., et al., 2016. A comparison of terrestrial laser scanning and structure-from-motion photogrammetry as methods for digital outcrop acquisition. Geosphere, 121865–1880.